The Impact of Cumulus Parameterization on Regional Climate Simulations of Central American Climate

JUSTIN GONZALEZ,[a,b] VASUBANDHU MISRA,[a,b] AND C. B. JAYASANKAR[b]

[a] *Department of Earth, Ocean and Atmospheric Science, Florida State University, Tallahassee, Florida*
[b] *Center for Ocean-Atmospheric Prediction Studies, Florida State University, Tallahassee, Florida*

(Manuscript received 19 December 2024, in final form 17 July 2025, accepted 24 July 2025)

ABSTRACT: In this study, we contrast and verify two coupled ocean–atmosphere regional climate simulations [RR–relaxed Arakawa–Schubert (RAS) and RR–Kain–Fritsch (KF)] spanning 15 years, at 15-km grid spacing, and centered over Central America that differ only in their cumulus parameterization schemes. The RAS scheme is based on quasi-equilibrium theory, and the KF scheme is based on an entraining/detraining plume model that triggers convection at a threshold CAPE. The model simulations are verified for their seasonal, subseasonal, and diurnal variations using reanalysis and other independent observations. The RR–KF scheme shows several notable improvements in the simulation relative to the RR–RAS scheme. These include a reduction of the terrestrial wet bias, improved representation of the ITCZ location in the eastern Pacific, reduction of the dry bias of the atmospheric column over the oceans, reduction of the westerly bias of the low-level trade winds, and improvement of the cold bias of the coastal SST. Despite these improvements, the bias in RR–KF simulations is still large and significant. It is encouraging to note that both simulations produced diurnal variability of rainfall, with its amplitude and phase verified reasonably well with corresponding observations. The simulation of the midsummer drought was comparable between the two simulations, with a verifiable gradient of its amplitude between the Pacific and the Caribbean coasts but with an underestimation of its frequency.

SIGNIFICANCE STATEMENT: The Central American region is a challenging region for climate simulation given its unique geography of a narrow isthmus with steep orography and neighboring oceans with significant variations across time scales. Most global circulation models with their current coarse horizontal resolution (~100-km grid spacing) are inadequate to resolve the frequently generated mesoscale convective systems and the many low-level jets in the region. Our study compares two coupled ocean–atmosphere regional climate model integrations at 15-km grid spacing forced with global reanalysis of the atmosphere and ocean that differ only in their cumulus parameterizations scheme. The results suggest that significant improvement in the regional climate simulation could be achieved by adopting a cumulus parameterization scheme based on the convective available potential energy closure assumption (Kain–Fritsch scheme) over a parameterization scheme based on quasi-equilibrium theory (relaxed Arakawa–Schubert scheme). These results could, however, be specific to the regional domain and the lateral boundary conditions used for the study. Despite these improvements, the model simulation with the Kain–Fritsch scheme continues to display significant bias, which requires further investigation.

KEYWORDS: Central America; Climatology; Coupled models; Climate variability; Diurnal effects; Tropical variability

1. Introduction

Central America presents one of the stiffest challenges for the simulation of regional climate features and their variability by numerical climate models (Rojas and Seth 2003; Giorgi 2006; Hidalgo and Alfaro 2015). This stems from its peculiar geography of an isthmus with steep topographic gradients and relatively warm tropical oceans on either side. The unique geography of Central America creates significant variations in atmospheric and oceanic conditions. These variations give rise to a wide range of climate and ecological zones throughout the region, making Central America one of the world's biodiversity hotspots (Myers et al. 2000).

The region's complex topography within the narrow isthmus, combined with the influence of the seasonally shifting easterly trade winds and meridional migration of ITCZ, results in a distinct seasonal precipitation pattern between the Pacific and Caribbean slopes (Magaña et al. 1999; Alfaro 2002; Taylor and Alfaro 2005; Amador et al. 2006). Along the Caribbean slope, precipitation maintains a consistent presence throughout the year, with biannual peaks in boreal winter and summer. These biannual peaks coincide with the seasonal changes in the strength of the Caribbean low-level jet (CLLJ; Davis et al. 1997; Amador 1998; Amador et al. 2000, 2006; Amador 2008; Muñoz et al. 2008; Durán-Quesada et al. 2017; Hidalgo et al. 2015; Sáenz et al. 2023). The CLLJ forms from the meridional sea level pressure gradient established by the North Atlantic subtropical high (NASH), further enhanced by the meridional temperature gradient between the relatively warm Greater Antilles and the cool Caribbean

---

Supplemental information related to this paper is available at the Journals Online website: https://doi.org/10.1175/JAMC-D-24-0240.s1.

Corresponding author: Vasubandhu Misra, vmisra@fsu.edu

DOI: 10.1175/JAMC-D-24-0240.1

Sea (Romero-Centeno et al. 2007; Wang 2007; Muñoz et al. 2008; Amador 2008). A schematic of the many different LLJs in the region is shown in Fig. S1 in the online supplemental material.

Similarly, the Pacific slope of Central America has its wet season in boreal summer and fall and the dry season in the boreal winter. This seasonal variability in precipitation is primarily dictated by the meridional migration of the ITCZ (Amador et al. 2006; Amador 2008; Hastenrath and Polzin 2013; Hidalgo et al. 2015; Sáenz et al. 2023). However, it is worth noting that other factors like the midsummer drought (MSD) also affect the seasonality of rainfall along the Pacific slope (Magaña et al. 1999; Taylor and Alfaro 2005; Amador et al. 2006; Amador 2008). During July and August, the Pacific slope of Central America experiences a local minimum of rainfall amid its rainy season, which is referred to as the MSD (or locally as veranillo or canícula).

The Choco jet (ChJ) is a moisture belt for the Pacific slope during the boreal fall, particularly in October and November (Poveda and Mesa 2000; Amador 2008; Durán-Quesada et al. 2017). The ChJ, first identified by Poveda and Mesa (2000), forms from the southerly cross-equatorial flow of the ITCZ (Fig. S1). Much of the moisture transport climatology in Central America can be understood as a seesaw mechanism between the NASH-enabled CLLJ, the ITCZ and ChJ, and the warm SSTs surrounding the landmass, in which these dynamical features dominate the region depending on the season (Durán-Quesada et al. 2017; Martinez et al. 2019). In the boreal winter and early summer, the CLLJ brings moisture from the Caribbean Sea and Atlantic ITCZ to the Caribbean slope, enabling widespread precipitation in this region while suppressing rainfall along the Pacific slope as its easterly winds flow over the continental divide. In the late boreal summer and autumn, as the CLLJ enters a weakened state and the east Pacific ITCZ enters its northernmost position, the ChJ and east Pacific ITCZ become dominant as they bring moisture from the south and west into the Pacific slope.

Beyond the CLLJ and ChJ, other LLJs play a key role in modulating the Central American climate system. These LLJs include the Papagayo jet (PpJ), a northeasterly jet off the Pacific coast of Nicaragua and Costa Rica, the Panama jet (PnJ), a northerly jet within the Gulf of Panama, and the Tehuantepec jet (TeJ), a northerly wind jet originating from the Isthmus of Tehuantepec (Fig. S1). The PpJ, PnJ, and TeJ are also called gap jets because they form from the channeling of the winds through gaps in the mountains. These jets are primarily active during the winter and early spring, in which southward intrusions of midlatitude cold air create significant meridional pressure gradients that cause winds to squeeze through these mountain gaps (Chelton et al. 2000a,b; Fiedler 2002; Muñoz et al. 2008; Misra and Jayasankar 2022). In addition, factors such as easterly waves and tropical cyclones also influence the PpJ and PnJ due to the changes they bring to the easterly trades (Chelton et al. 2000a,b). Regarding their impacts on the regional climate of Central America, the PpJ and TeJ are noted to play a role in the seasonal development of the Costa Rica Dome, a dome of shoaling thermoclines that sustain high biological productivity along the Pacific coast (Fiedler 2002). Furthermore, these jets are found to aid in the reinvigoration or development of tropical easterly waves. For example, in some instances, the CLLJ and PpJ cause a sign reversal of the meridional potential vorticity gradient at 700 mb (1 mb = 1 hPa), creating a barotropically unstable environment suitable for growth or generation of easterly waves (Charney and Stern 1962; Molinari et al. 1997). Similarly, the PpJ and ChJ are known to provide moisture and low-level vorticity within precursor mesoscale convective systems such as those found in the Panama Bight, enabling easterly wave formation and their reinvigoration (Holbach and Bourassa 2014; Whitaker and Maloney 2020).

The eastern Pacific Ocean and the Caribbean Sea also serve as hosts for a key notable feature of the region, the Western Hemisphere warm pool (WHWP) (Wang and Enfield 2001; Amador et al. 2006; Amador 2008). The WHWP is a pool of sea surface temperatures at or exceeding 28.5°C which at its greatest areal extent consists of portions of the eastern tropical North Pacific, Gulf of Mexico, Caribbean Sea, and western North Atlantic. The WHWP first develops in the eastern tropical North Pacific during the early boreal spring and gradually expands into the Intra-Americas Seas as the boreal summer begins and incoming shortwave flux, which fuels its growth, increases (Wang and Enfield 2001). The WHWP is important to note, for one, due to its association with organized tropical convection such as easterly waves and tropical cyclones, since it is generally correlated with reduced vertical shear, sea level pressure, and static stability (Hidalgo et al. 2020). Additionally, the warm SSTs of the WHWP, in conjunction with the barotropic instability provided by the regional LLJs, create a favorable environment for easterly wave formation like that seen off the western coast of Africa (Núñez Ocasio et al. 2020a, 2021; Rajasree et al. 2023).

On a more local scale, land–sea breezes are a primary driver of diurnal rainfall variability, another facet of Central America's climate (Giannini et al. 2000; Taylor and Alfaro 2005; Hidalgo et al. 2015; Maldonado et al. 2018). These land–sea breezes are most prominent in the boreal summer (Garreaud and Wallace 1997; Mapes et al. 2003a,b; Curtis 2004; Vera et al. 2006; Diro et al. 2012). Observational analysis, such as that of Curtis (2004), reveals an alternating pattern in which diurnal rainfall over the Central American landmass contains nocturnal peaks (1800–0300 LST), while the eastern Pacific contains daytime peaks (0600–1500 LST). These results were further affirmed by Diro et al. (2012), which showed with the finer resolutions of the TRMM 3B42 dataset that the diurnal peak of rainfall over Central America in the summer season is around 2100 LST or later, while over the surrounding oceans, the gradients of the time of the diurnal rainfall peak are relatively larger (ranging from ~0000 to 1800 LST). Furthermore, Diro et al. (2012) show that diurnal variations explained nearly 70% of the daily variance during the boreal summer season over the region, making this temporal scale key to studying Central American summer climatology. In addition, they indicate that the diurnal variation in precipitation in the boreal summer season is higher over Central America, with the oceans containing a fraction of the diurnal rainfall amplitude over the land, except in the Gulf of Panama and along the coastal ocean of Colombia where it is comparable or even exceeds the terrestrial diurnal amplitude.

There are several other climate modulators for Central America which exist beyond the regional scale, one such example being ENSO. For instance, Giannini et al. (2000) found that ENSO likely has a multifaceted impact on climate variability in the region that varies depending on the ENSO mode, in which changes to synoptic pressure features, wave train shapes, and SST anomalies lead to enhanced or suppressed seasonal rainfall. Furthermore, since Central America acts as a bridge for the North and South American continents, its climate is intrinsically connected to that of these continents. For instance, the North American monsoon system facilitates rainfall during the Central American wet season as it enables an intensification of easterly trade winds, while the moisture transport brought by the ChJ and east Pacific ITCZ near northwestern South America influences precipitation along the Pacific coast of Central America (Vera et al. 2006; Maldonado et al. 2018; Prein et al. 2024). Variability in these external climate features, in addition to others not explicitly mentioned such as tropical North Atlantic SSTs (Misra et al. 2014; Durán-Quesada et al. 2017, 2020) and subtropical highs in both ocean basins (Rodgers et al. 2024), creates a complicated picture of Central America's climate when also considering the previously mentioned local and regional factors. Therefore, predicting the seasonal hydroclimate in the region proves a challenging endeavor (Alfaro et al. 2018; Misra and Jayasankar 2022, hereafter MJ22; Kowal et al. 2023; Rodgers et al. 2024).

The regional climate of Central America poses a significant challenge to the general circulation models (GCMs) to simulate and project its climate (Hidalgo and Alfaro 2015; Maldonado et al. 2018; Almazroui et al. 2021). Its several mesoscale features both over the land and ocean including its topography and bathymetry are often poorly resolved in the coarse-resolution GCMs (MJ22). Therefore, as an alternative, higher-resolution regional climate models (RCMs) forced by some of these coarsely resolved GCMs at the lateral boundaries are one of the strategies used to simulate the climate over Central America (Cabos et al. 2019; Martínez-Castro et al. 2018; Cavazos et al. 2020; Corrales-Suastegui et al. 2020). However, many of these studies conducted with RCMs are at around 50-km grid resolution (e.g., Cavazos et al. 2020; Corrales-Suastegui et al. 2020), while some are relatively finer at ~25-km grids (e.g., Karmalkar et al. 2011; Cabos et al. 2019). However, all these studies are conducted from downscaling only the atmospheric component using a regional atmospheric model with few exceptions using a regional coupled ocean–atmosphere model (e.g., Li and Misra 2014; Cabos et al. 2019; MJ22). From a practical standpoint, high-resolution Earth system models are preferred numerical tools for predicting or projecting a coupled climate system, wherein, its various components are coevolving through exchange of fluxes or state variables at their interface (Shapiro et al. 2010; Brown et al. 2012).

In this study, we compare the regional coupled ocean–atmosphere simulation in MJ22 with another simulation from an identical model setup, with only the cumulus parameterization scheme in the atmospheric component of the RCM being altered. Earlier intercomparison studies of cumulus parameterization schemes over Central America were conducted in regional atmosphere models where SST was prescribed (e.g., Mapes et al. 2004; Martínez-Castro et al. 2018; Rivera et al. 2022). These studies find that none of the cumulus parameterization schemes serve as a panacea for the model precipitation and associated circulation bias in the region. Nonetheless, they all note that cumulus parameterization has a significant impact on the simulation of the Central American climate. This study is unique in that the cumulus parameterization scheme is being tested in a regional coupled ocean–atmosphere modeling framework centered over Central America. The coupled ocean–atmosphere modeling framework is a more realistic setup to compare, where the parameterized deep convection is interacting across spatiotemporal scales and with all components of the climate system as coupled air–sea feedback could be nonlinear and at times counterintuitive (Misra and Marx 2007).

In the following section, we describe the model followed by the description of the design of experiments in section 3. The results are discussed in section 4 followed by conclusions in section 5.

2. Model description

The model utilized in this study is the Regional Spectral Model–Regional Ocean Modeling System (RSM–ROMS), which is identical to that used in MJ22. RSM–ROMS is a regional, coupled ocean–atmosphere model that has been widely employed in regional climate modeling research spanning many regional domains around the globe (Li et al. 2014; Li and Misra 2014; Ham et al. 2016; Misra et al. 2018). The atmospheric component of RSM–ROMS is RSM, which was initially introduced in Juang and Kanamitsu (1994). RSM utilizes the spectral method to calculate advective derivatives using sine and cosine functions in two dimensions with wall boundary conditions (Tatsumi 1986). RSM employs a semi-implicit time integration scheme and consists of 28 terrain-following sigma levels with irregular vertical spacing that mirrors the National Centers for Environmental Prediction-Department of Energy (NCEP-DOE) reanalysis, version 2 (R2; Kanamitsu et al. 2002), with the top of the atmosphere in RSM located at approximately 2 hPa. The scale-selective bias correction method following Kanamitsu et al. (2010) is implemented to mitigate synoptic-scale drift in the integration of the RSM. The width of the sponge zone surrounding the lateral boundaries is 16 grid points. The physics package utilized in RSM for this study is detailed in Table 1.

The only difference between the version of the RSM–ROMS used in MJ22 and in this study is that in the former, the relaxed Arakawa–Schubert (RAS) scheme (Moorthi and Suarez 1992) is used, and in the latter, the Kain–Fritsch (KF; Kain and Fritsch 1993; Kain 2004) cumulus parameterization is used. The version of KF used in this study is version 2 (KF2), which is an improvement over its previous version (Kain and Fritsch 1993) in that KF2 incorporates a more detailed cloud model, which makes the scheme to be more sensitive to boundary layer processes and moisture availability, improves its entrainment/detrainment, utilizes a better closure assumption, and incorporates an enhanced convective momentum transport. Henceforth, KF2 will be referred to as KF

TABLE 1. Outline of RSM physics package.

Physical process parameterized	Reference
Boundary layer	Hong and Pan (1996)
Prognostic clouds	Zhao and Carr (1997)
Gravity wave drag	Alpert et al. (1988)
Longwave radiation	Chou and Lee (1996)
Shortwave radiation	Chou and Suarez (1994)
Land surface model	Ek et al. (2003)
Deep convection	Kain and Fritsch (1993)
Shallow convection	Tiedtke (1983)
Cloud cover	Sundqvist et al. (1989), Slingo (1987)

in this paper. The KF and RAS schemes are two commonly adopted schemes in many climate models (Yang and Wang 2019; Budakoti et al. 2019; Chen et al. 2021). In the case of RSM–ROMS, we have used these two schemes in different instances, each providing reasonable results (Selman and Misra 2015; Glazer and Misra 2018; Bhardwaj and Misra 2019; Misra and Jayasankar 2022, 2025). But a comparison of these two cumulus parameterization schemes in RSM–ROMS has thus far been lacking. The fundamental differences between the two schemes are outlined in Table 2.

ROMS is the oceanic component of RSM–ROMS following Haidvogel et al. (2000) and Shchepetkin and McWilliams (2005). ROMS is a free surface, terrain-following primitive equation model, which uses a split explicit time-stepping scheme. To discretize the primitive equations in the vertical direction, ROMS utilizes stretched, terrain-following coordinates with 30 levels. In addition, ROMS incorporates several subgrid-scale parameterizations like the local closure schemes based on the level 2.5 turbulent kinetic energy equations developed by Mellor and Yamada (1982), generic length-scale parameterization (Umlauf and Burchard 2003), the second-order biharmonic horizontal diffusion (Ezer et al. 2002), and the nonlocal closure scheme based on the *K*-profile boundary layer formulation (Large et al. 1994) for both surface and bottom oceanic boundary layers.

The coupling interval of RSM–ROMS is 1 h. The atmospheric fluxes and SST are directly exchanged between RSM–ROMS without the use of any flux coupler as they share identical grids. In addition, no flux corrections are applied during the integration.

3. Experiment design

The regional model domain used for this study is identical to MJ22 and is shown in Fig. 1e, with RSM–ROMS at 15-km grid spacing. The RSM model receives initial and lateral boundary conditions for the atmosphere from R2 reanalysis (Kanamitsu et al. 2002). The lateral boundary conditions for RSM are updated every 6 h. The ocean initial and lateral boundary conditions are sourced from the Simple Ocean Data Assimilation, version 2.4 (SODAv2.4; Carton and Giese 2008). The RSM–ROMS model is integrated for the period from 1 January 1986 to 31 December 2001. Hereafter, the RSM–ROMS integration of this study will be referred to as RR–KF and that of MJ22 as RR–RAS. The validation datasets used for this study are outlined in Table 3. The model biases are computed on the observations/reanalysis grid.

4. Results

a. Seasonal climatology

In Fig. 1, we show the seasonal mean precipitation from both model simulations and their comparison with the corresponding observations and each other. There are large, significant differences between the two simulations both over the terrestrial and oceanic regions of the domain. For example, the terrestrial wet bias of RR–RAS is reduced in RR–KF across all seasons. Similarly, there is some improvement in the location of the ITCZ over the eastern Pacific Ocean in RR–KF relative to RR–RAS. For example, the erroneous northward displacement in the RR–RAS simulation is slightly

TABLE 2. Key differences between RAS and KF schemes.

Feature	RAS	KF
Concept	Based on quasi-equilibrium theory: convection acts to maintain equilibrium between large-scale forcing and the cloud ensemble.	Is a mass flux scheme, which focuses on triggering convection when certain criteria of instability and moisture availability are met.
Triggering of convection	There is no explicit triggering of convection. Convection is continuously active to relax the instability over time.	There is explicit triggering of convection in the presence of exceeding a threshold of convectively available potential energy and moisture convergence.
Closure mechanism	Based on the quasi-equilibrium theory.	Based on stabilizing the atmosphere by removing the CAPE.
Adjustment	Gradual over a relaxation time scale of half hour.	Rapid onset of convection once the triggering conditions are met.
Cloud representation	A spectrum of cloud types with different detrainment levels.	The scheme uses a single-column convective cloud model that explicitly calculates the mass flux and entrainment/detrainment of air between the convective updraft (and downdraft) and the surrounding environment.

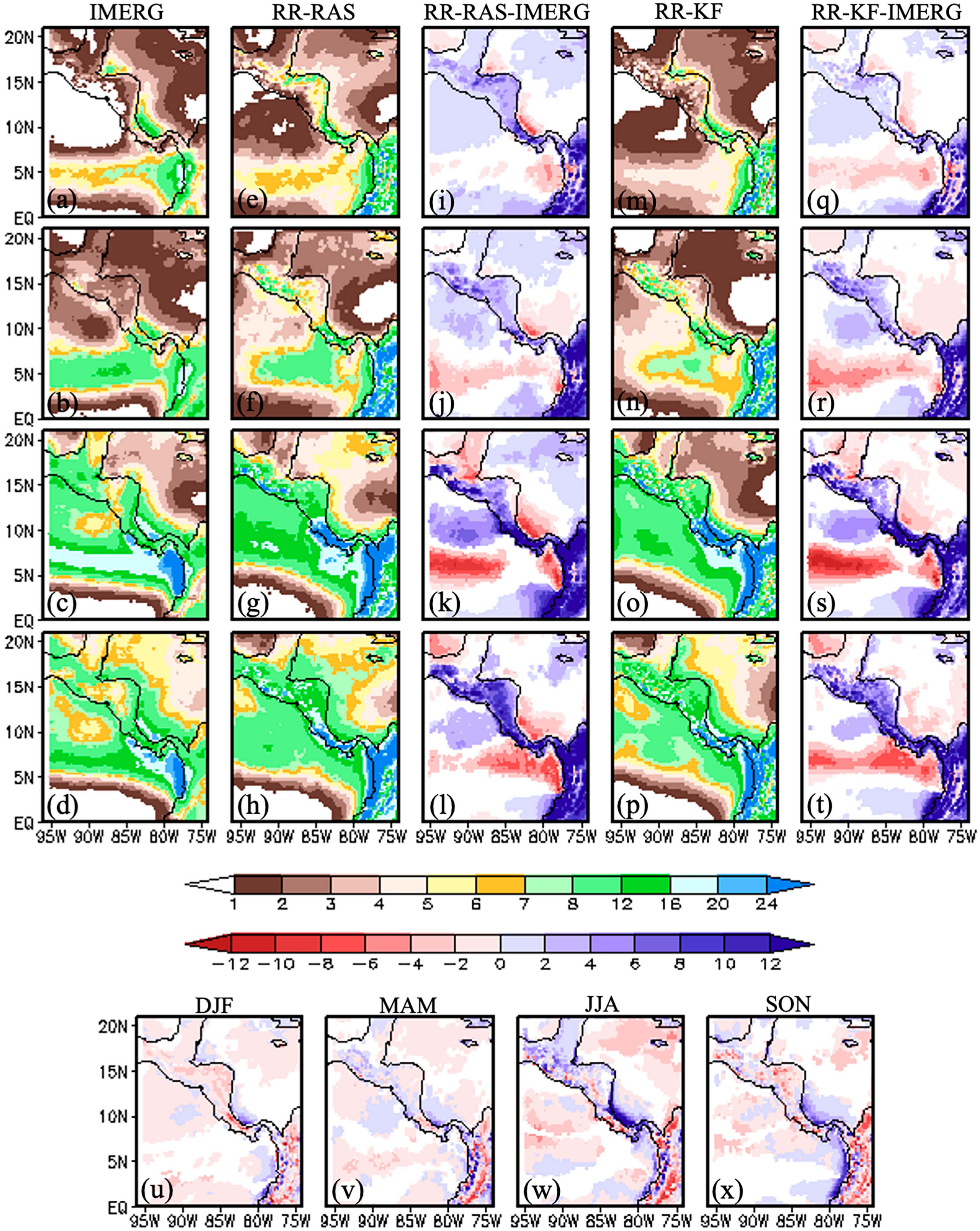

FIG. 1. The climatological seasonal mean rainfall (mm day^{-1}; shaded) from (a)–(d) observations (IMERG), (e)–(h) RR–RAS, (i)–(l) systematic errors of RR–RAS, (m)–(p) RR–KF, and (q)–(t) systematic errors of RR–KF for (a),(e),(i),(m),(q) DJF, (b),(f),(j),(n),(r) MAM, (c),(g),(k),(o),(s) JJA, and (d),(h),(l),(p),(t) SON seasons. The corresponding climatological seasonal mean difference of precipitation between the model simulations: (RR–KF) − (RR–RAS) for (u) DJF, (v) MAM, (w) JJA, and (x) SON seasons. The differences are shaded in (i)–(l) and (q)–(x) only if they exceed the 95% confidence interval.

TABLE 3. Verification datasets used in the study.

Variable	Source	Purpose	Spatial resolution	Period used in the study
Rainfall	IMERG v7 (Huffman et al. 2023, 2024)	Verification of seasonal mean, diurnal, and intraseasonal variations of precipitation over both land and ocean	0.1° × 0.1°	2001–23
SST	OISSTv2 (Reynolds et al. 2007)	Verification of SSTs	0.1° × 0.1°	1986–2001
Enthalpy fluxes	OAFlux (Yu et al. 2008)	Verification of latent and sensible heat flux	1° × 1°	1986–2001
Upper-air variables and precipitable water	ERA5 (Hersbach et al. 2019)	Verification of the winds at 850 and 925 hPa, LLJs, and precipitable water	0.5° × 0.5°	1986–2001

reduced across all seasons in the RR–KF simulation. However, the dry bias over portions of the open Caribbean Sea is slightly exacerbated in RR–KF compared to RR–RAS. However, the severe dry bias along the Caribbean coasts of Panama and Costa Rica in RR–RAS is substantially reduced in RR–KF. RR–KF also contains a similar open ocean dry bias in the east Pacific, which is more severe near 5°N than RR–RAS. These qualitative observations are confirmed in the quantitative estimates shown as pattern correlations and standardized variance in the Taylor diagram in Fig. S2a. The superiority of the spatial distribution of precipitation in RR–KF over RR–RAS in terms of pattern correlation and standardized variance is apparent in Fig. S2a. However, both models exhibit stronger gradients and weaker pattern correlations of terrestrial precipitation than observations, while they are more comparable over the oceans.

Further analysis of the surface rainfall climatology is depicted in Figs. S3 and S4. Figure S3 shows that RR–KF produces higher convective rainfall than RR–RAS within the Central American landmass and along the coasts. In contrast, the differences in the stratiform precipitation are uniformly lower across the domain in RR–KF relative to RR–RAS, with the most acute differences appearing along the Pacific ITCZ in the JJA season and along elevated terrestrial regions (Fig. S4). It may be noted that the precipitation along the Pacific ITCZ (Feng et al. 2025) and over topographic regions (Hamilton et al. 2017, 2020) are often not well captured or resolved in parameterized simulations. The Pacific coast of the isthmus is commonly associated with short-lived, intense, yet organized mesoconvective rainfall due to forcings such as sea breezes, orographic lifting, diurnal variability, and convection coupled to easterly waves (Velasco and Fritsch 1987; Poveda and Mesa 2000; Alfaro 2002; Mapes et al. 2003a; Whitaker and Maloney 2020; Núñez Ocasio et al. 2020b; Jenney et al. 2025). Recalling that terrestrial and coastal locations were areas where RR–KF improved upon RR–RAS in the surface rainfall climatology (Fig. 1), it follows that the physics of RR–KF may provide a more accurate simulation of rainfall in terrestrial and coastal regions, where mesoscale and synoptic-scale features interact with environmental parameters such as moisture convergence and CAPE, that then play a prominent role in convection initiation.

Similarly, the comparisons of the model simulations of seasonal mean precipitable water are shown in Fig. 2. The biases in precipitable water are comparable in both simulations of RSM-ROMS across all seasons. For example, the wet bias over the land in the boreal winter and spring seasons and the dry bias over the oceans are comparable in RR–RAS and RR–KF. Although over the oceans, the dry bias is slightly ameliorated in RR–KF relative to RR–RAS (Figs. 2u–x). The corresponding Taylor diagram in Fig. S2b for precipitable water unlike in Fig. S2a for precipitation shows that the standardized variance is less than 1 across the domain, suggesting weaker spatial gradients in the model simulations compared to ERA5 with both RSM–ROMS simulations being comparable to each other. Furthermore, the pattern correlations of precipitable water are higher than those for precipitation in Fig. S2a, and these pattern correlations are much larger over the oceans than over the land for both model simulations (Fig. S2b).

The seasonal climatology of SST in Fig. 3 shows some large improvements along the coastal oceans in RR–KF compared to RR–RAS. For example, the persistent cold SST bias in the Gulf of Panama, Venezuelan Coast, and the cold SST bias appearing in the boreal summer and fall seasons along the Pacific coast of Central America in RR–RAS is significantly reduced in RR–KF. However, the warm bias in the RR–KF away from the coastal regions in the Caribbean Sea and in the eastern Pacific is exacerbated relative to RR–RAS. The corresponding Taylor diagram computed over all ocean grid points in the domain in Fig. S2c shows the superiority of RR–KF with respect to RR–RAS in terms of standardized variance and modest improvement in pattern correlations across all seasons, especially in the winter and spring seasons.

Further insight into these differences in SST between the simulations could be obtained from the corresponding differences in the cloud cover (Figs. S5 and S6). It is observed that the RR–KF and the RR–RAS simulations produce contrasting differences in the low-level (Fig. S5) and upper-level (Fig. S6) cloud cover, with RR–KF producing uniformly less low-level cloud cover and more upper-level cloud cover than RR–RAS across all seasons. In comparison, the midlevel cloud-cover differences between the models were far less (not shown). The reduced low-level cloud cover in RR–KF would allow increased shortwave radiation to reach the surface, supporting warming at the ocean surface. The relatively higher upper-level cloud cover in RR–KF would then reinforce the surface warming feedback by trapping outgoing longwave radiation. These systematic changes in cloud cover suggest that the convection in the RR–KF simulation could support a warmer

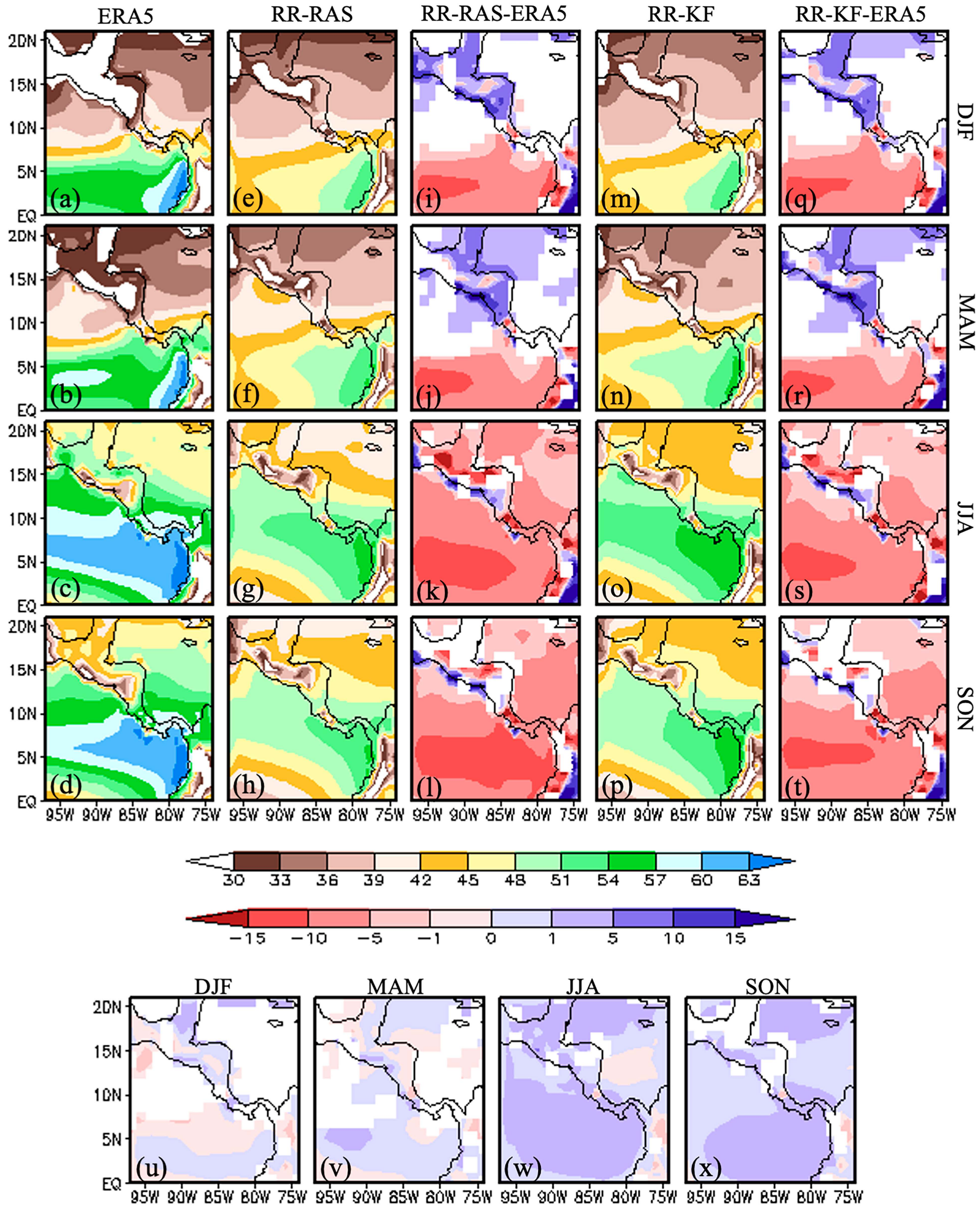

FIG. 2. The climatological seasonal mean precipitable water (kg m^{-2}; shaded) from (a)–(d) observations (ERA5), (e)–(h) RR–RAS, (i)–(l) systematic errors of RR–RAS, (m)–(p) RR–KF, and (q)–(t) systematic errors of RR–KF for (a),(e),(i),(m),(q) DJF, (b),(f),(j),(n),(r) MAM, (c),(g),(k),(o),(s) JJA, and (d),(h),(l),(p),(t) SON seasons. (u)–(x) The corresponding climatological seasonal mean difference of precipitation between the model simulations: (RR–KF) − (RR–RAS). The differences in (i)–(l) and (q)–(x) are shaded only if they exceed the 95% confidence interval.

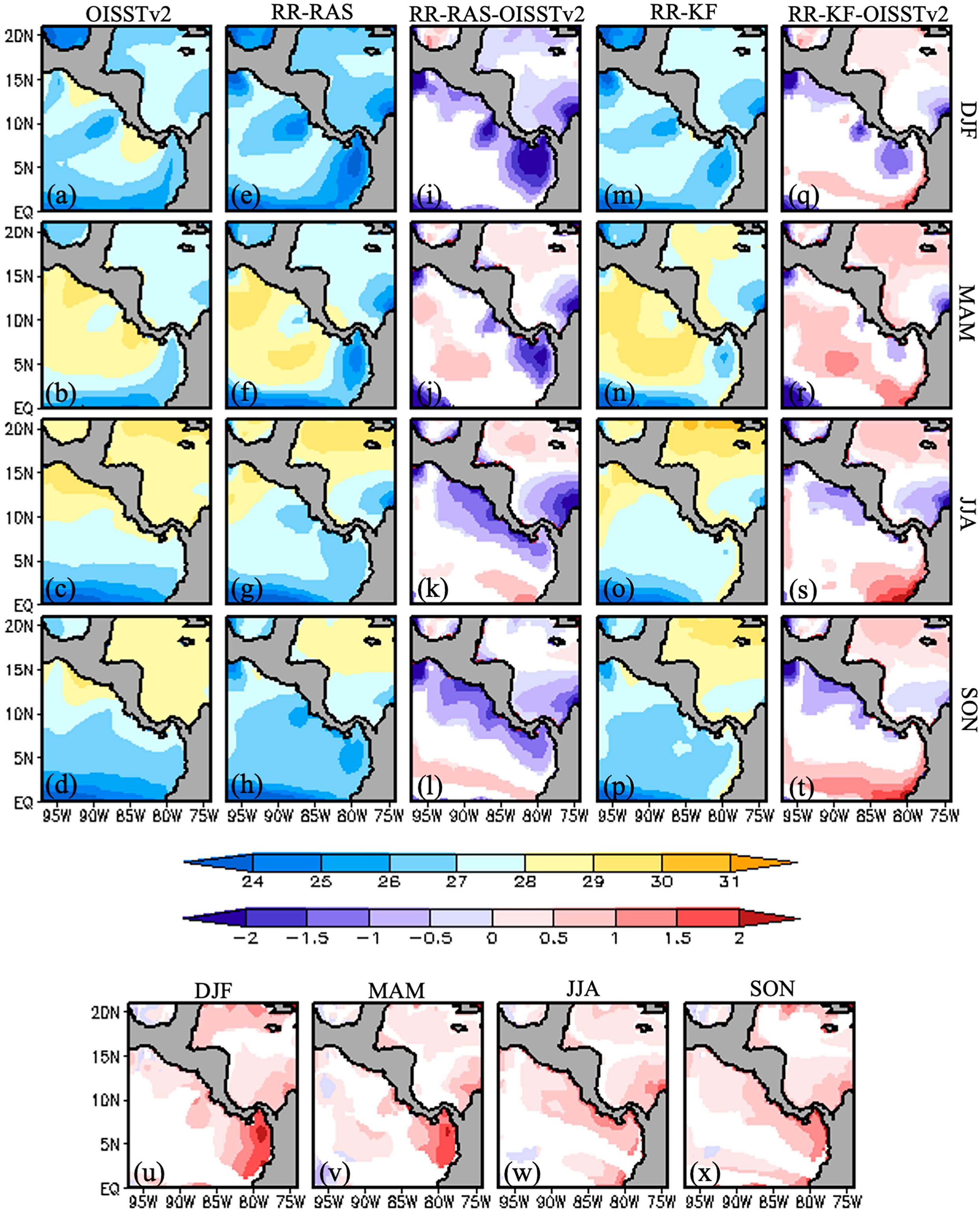

FIG. 3. The climatological seasonal mean SST (°C; shaded) from (a)–(d) observations (OISSTv2), (e)–(h) RR–RAS, (i)–(l) systematic errors of RR–RAS, (m)–(p) RR–KF, and (q)–(t) systematic errors of RR–KF for (a),(e),(i),(m),(q) DJF, (b),(f),(j),(n),(r) MAM, (c),(g),(k),(o),(s) JJA, and (d),(h),(l),(p),(t) SON seasons. (u)–(x) The corresponding climatological seasonal mean difference of precipitation between the model simulations: (RR–KF) − (RR–RAS). The differences in (i)–(l) and (q)–(x) are shaded only if they exceed the 95% confidence interval.

surface over oceanic and terrestrial points compared to RR–RAS simulation, which results in the reduction of the cold SST bias in the former, such as that seen along the Pacific coast of Central America and the Gulf of Panama (Fig. 3). However, it is important to note that wind-driven oceanic mixing may also play a role in regulating SSTs.

The seasonal mean 925-hPa winds are shown in Fig. 4. In ERA5, an axis of converging winds associated with the ITCZ can be seen south of 10°N (Figs. 4c,d). But RR–RAS and RR–KF simulations place this axis at ~10°N, suggesting a northward push of the ITCZ (Figs. 4g,h and 4o,p). This bias is further confirmed in the corresponding biases of the 925-hPa winds of RR–RAS (Figs. 4k,l) and RR–KF (Figs. 4s,t) in which both models place a notable southwesterly wind bias along the same latitude as the ITCZ in ERA5, pushing this feature northeast toward the landmass. The corresponding Taylor diagram in Fig. S2d shows a significant improvement in the pattern correlation and the variance of the zonal winds in RR–KF compared to RR–RAS.

The region is well known for several LLJs including the Caribbean, Papagayo, Choco, Panama, and the Tehuantepec LLJs (Fig. S1). Of these, the PpJ, PnJ, and TeJ are considered gap jets because they form from the easterly winds channeling through the gaps in the mountain ranges (Xie et al. 2005; Romero-Centeno et al. 2007). While most of these LLJs have their core at 925 hPa, they are also identifiable at 850 hPa (Fig. 5; Mora 2017; Yepes et al. 2019; Torres-Alavez et al. 2021). The monthly climatological time series of LLJ indices (defined in the caption of Fig. 5) and their corresponding cross sections are quite similar between RR–RAS and RR–KF (Fig. 5). The latitudinal and longitudinal locations and wind speeds of the LLJ cores during their annual peaks shown in the climatological monthly mean vertical cross sections in Figs. 5f–j match quite well with the earlier observational studies using remotely sensed wind products and in situ measurements from field campaigns (e.g., Holbach and Bourassa 2014; Mora 2017; Yepes et al. 2019).

The seasonal cycle of the CLLJ and the PpJ in Figs. 5a and 5b shows their seasonal peaks in boreal summer and winter, indicating both models adequately replicate their seasonal behavior. This seasonal cycle of the PpJ is linked to the seasonal variations of the Caribbean high and meridional migration of the eastern Pacific ITCZ (Wang and Lee 2007; Muñoz et al. 2008). These two zonal jets are the strongest in the region with the CLLJ displaying a core strength of 14 m s^{-1} (Fig. 5f; Torres-Alavez et al. 2021) being slightly stronger than the PpJ with its core strength at 10 m s^{-1} (Fig. 5g; Yepes et al. 2019).

The northerly PnJ is stronger in boreal winter, which is also observed in both model simulations (Figs. 4, and 5c,5h). Unlike the CLLJ or the PpJ, the PnJ can disappear or become significantly weak in summer (Fig. 5c; Chelton et al. 2001; Amador 2008; Mora 2017). This is because in summer, the eastern Pacific ITCZ shifts further north, reducing the meridional pressure gradient, which combined with reduced easterlies from the Caribbean limits the development of strong gap flow.

The ChJ has a seasonal peak in the boreal fall season (Fig. 5d; Poveda and Mesa 2000; Yepes et al. 2019), which is seen as a westerly flow of the Colombian coast. The ChJ is westerly and is the weakest compared to the other zonal jets in the region, being primarily associated with the SST gradients between the Niño-1 + 2 region and the Colombian Pacific coast (Poveda and Mesa 2000). The slightly stronger simulation of the ChJ in RR–KF (Figs. 5d,i) is a key improvement in the wind field simulation, since this jet is a conduit of vital moisture to the Pacific coast of Colombia during the fall season (Poveda and Mesa 2000; Durán-Quesada et al. 2017), which has shown considerable improvement in the dry bias of RR–RAS (Fig. 1x).

The northerly TeJ also has a seasonal peak in the boreal winter and a notable decrease in the summer (Fig. 5e). The seasonal peak in the winter is associated with the southward movement of cold frontal systems from North America into the Gulf of Mexico with the associated winds channeled through the Chivela Pass in Mexico, accelerating the cooler, denser air toward the Pacific Ocean (Romero-Centeno et al. 2003).

At 850-hPa pressure level, the westerly bias of RR–RAS over the Caribbean Sea is reduced in RR–KF but exacerbated in eastern Pacific (Fig. S7). Additionally, the northeasterly winds in the reanalysis are more easterly in both the model simulations over the east Pacific. The Taylor diagram computed over all grid points in the domain in Fig. S2e shows that the zonal winds have higher pattern correlations in both model simulations than the meridional winds in JJA and SON seasons. However, the skills in terms of the pattern correlations and standardized variance are comparable in both models across all seasons for the 850-hPa winds (Fig. S2e).

Further evidence of the impact of these cumulus parameterization schemes on the oceans can be seen in the comparisons of the latent heat flux over the oceans in Fig. 6 in which RR–KF generates more latent heat flux than RR–RAS in all seasons. This reduces the bias considerably over the oceans in the boreal winter season in RR–KF and along the coasts of Venezuela and the Pacific coast of Central America throughout the year but exacerbates the errors in the boreal spring season and over the open eastern Pacific Ocean and Caribbean Sea compared to RR–RAS.

Similarly, RR–KF also exhibits higher sensible heat flux over the oceans compared to RR–RAS except over the eastern Pacific Ocean in the boreal winter and spring seasons (Fig. 7). This change substantially reduces the weak sensible heat flux bias in the oceans in RR–RAS. This rectification of the sensible heat flux in RR–KF is seen in both the open and the coastal oceans.

b. *Diurnal variability of precipitation*

We isolate the local diurnal harmonic following Dai and Wang (1999). The harmonic analysis of a time series is done by the decomposition of a periodic function into a sum of trigonometric functions like

$$R(t) = R_o + \sum_{i=1}^{N/2} A_i \cos(i\theta - \Phi_i), \tag{1}$$

where N, R_o, A_i, and Φ_i are the number of intervals (=24 for hourly) and daily mean value of the variable, amplitude, and phase angle of the ith harmonic (with $i = 1$ corresponding

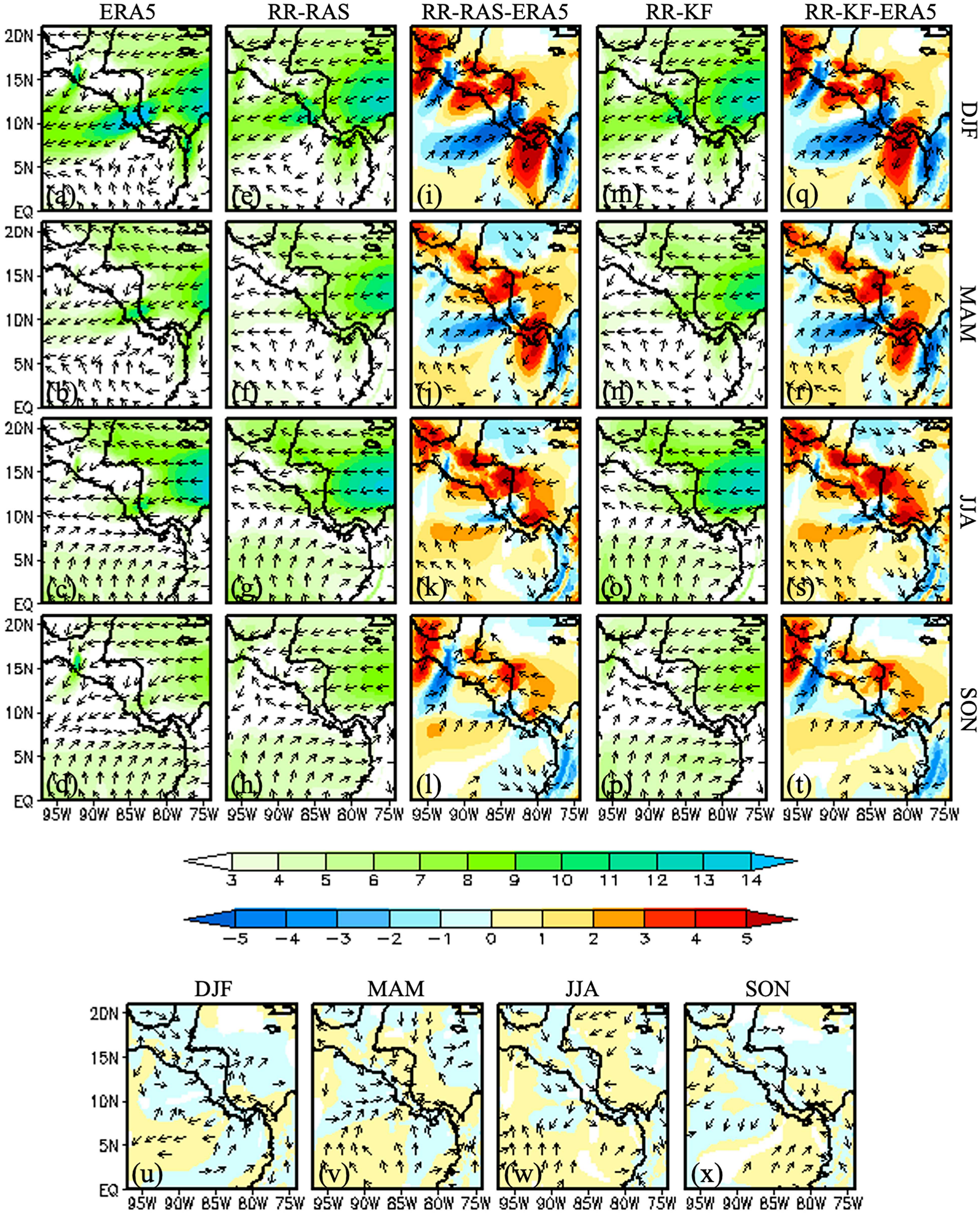

FIG. 4. The climatological seasonal mean 925-hPa winds (m s^{-1}) from (a)–(d) observations (ERA5), (e)–(h) RR–RAS, (i)–(l) systematic errors of RR–RAS, (m)–(p) RR–KF, and (q)–(t) systematic errors of RR-KF for (a),(e),(i),(m),(q) DJF, (b),(f),(j),(n),(r) MAM, (c),(g),(k),(o),(s) JJA, and (d),(h),(l),(p),(t) SON seasons. (u)–(x) The corresponding climatological seasonal difference of (RR-KF) − (RR-RAS). The vectors in (i)–(l) and (q)–(x) are shown only if they exceed the 95% confidence interval.

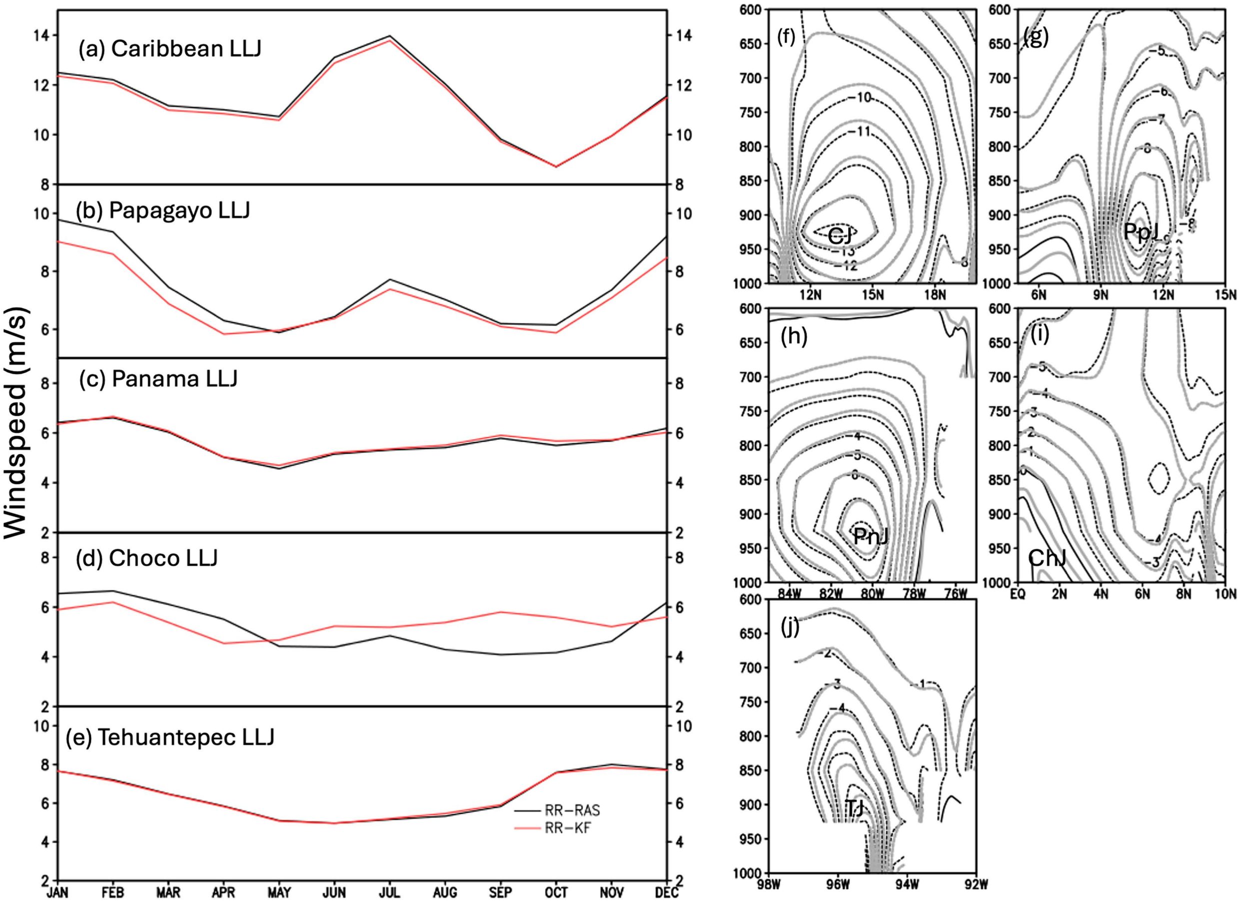

FIG. 5. The climatological monthly mean time series of the indices of the (a) Caribbean (78°–78°W and 13°–15°N), (b) Papagayo (89°–85°W and 9°–11°N), (c) Panama (80°–78°W and 3°–7°N), (d) Choco (80°–78°W and 1°–4°N), and (e) Tehuantepec (96°–94°W and 15°–17°N) LLJs. These indices are computed at 925 hPa. The corresponding monthly mean climatological vertical cross section in the lower troposphere from 1000 to 600 hPa at their month of annual peak for the (f) zonal wind of the CLLJ at 75.5°W in July, (g) zonal wind of the PpJ at 87°W in January, (h) meridional wind of the PnJ at 5°N in February, (i) zonal wind of the ChJ at 80°W in February, and (j) meridional wind of the TeJ at 16°N in November. The dotted black and solid gray contour lines in (e)–(j) correspond to RR-RAS and RR-KF, respectively. The contour interval is 1 m s^{-1} in (e)–(j).

to diurnal harmonic), respectively, and $\theta = (2\pi t_k)/N$, $t_k = \{00, 01, 02, 03, \ldots, 24\}$. There is a growing consensus that a good simulation of the diurnal cycle is necessary for representing the regional climate of the region (Yang and Slingo 2001; Diro et al. 2012; Martínez-Castro et al. 2018). The results of Diro et al. (2012) and Curtis (2004) discussed previously are largely reaffirmed from the half-hourly IMERG observations in Fig. 9 and Fig. S9 for JJA and SON seasons, respectively.

In JJA, the IMERG observations in Fig. 8a indicate that the diurnal amplitude of rainfall is over 6 mm day^{-1} across Central America except for a transect from western Nicaragua through northern Honduras, where it is below 6 mm day^{-1}. Interestingly, the oceans just west of Colombia exhibit a strong diurnal amplitude with rain rates over 27 mm day^{-1}. Poveda and Mesa (2000) indicate that the Colombian Pacific coast experiences on average 8000–13 000 mm of average annual precipitation, which makes it the rainiest locality on Earth. It may, however, be mentioned that Shige et al. (2017) suggest that infrared-based rainfall estimates used in the IMERG rainfall dataset tend to erroneously smear rainfall in the coastal oceans upstream of orography. Furthermore, the amplitude of the rainfall over the eastern Pacific Ocean and in the Mosquito Gulf in the Caribbean Sea has diurnal amplitudes exceeding 13 mm day^{-1}. The corresponding simulations from RR–RAS (Fig. 8b) and RR–KF (Fig. 8c) show close correspondence to the observations (Fig. 8a). However, both models show a tendency to overestimate the diurnal amplitude over the terrestrial regions and underestimate over the neighboring oceans. The corresponding verification of the phase of the diurnal cycle of precipitation in Figs. 8d–f suggests that the models are doing a reasonable job in simulating this feature. For example, the contrast in the peak of the diurnal rainfall over the eastern Pacific Ocean and terrestrial Central America is picked quite well in both model simulations. However, both models show a tendency for the peak diurnal rainfall to occur in the early morning hours in

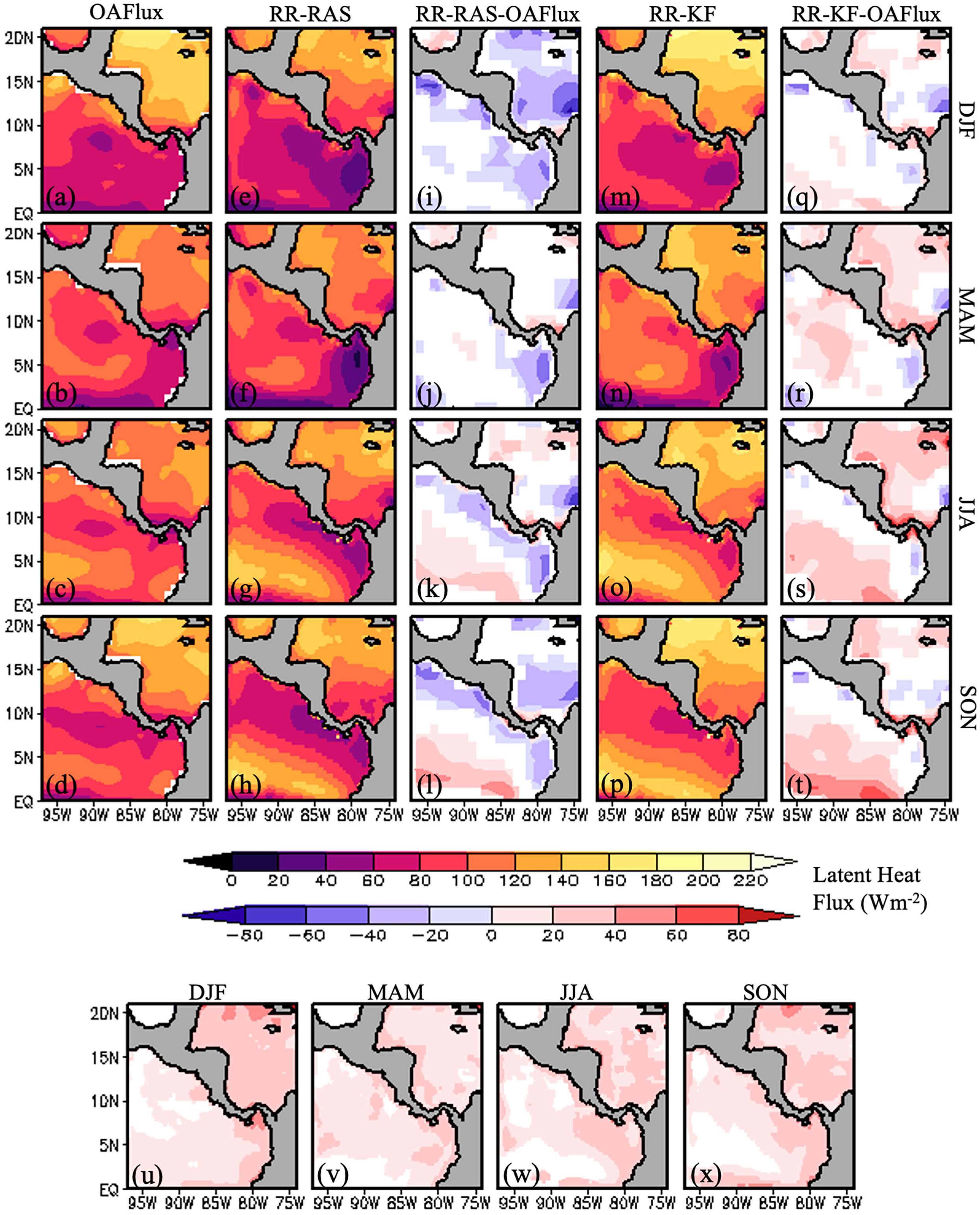

FIG. 6. The seasonal mean climatological surface latent heat flux (W m^{-2}; shaded) from (a)–(d) observations (OAFlux), (e)–(h) RR-RAS, (i)–(l) systematic errors of RR-RAS, (m)–(p) RR-KF, (q)–(t) systematic errors of RR-KF, and (u)–(x) difference of (RR-KF) − (RR-RAS). The differences in (i)–(l) and (q)–(x) are shaded only if they exceed the 95% confidence interval.

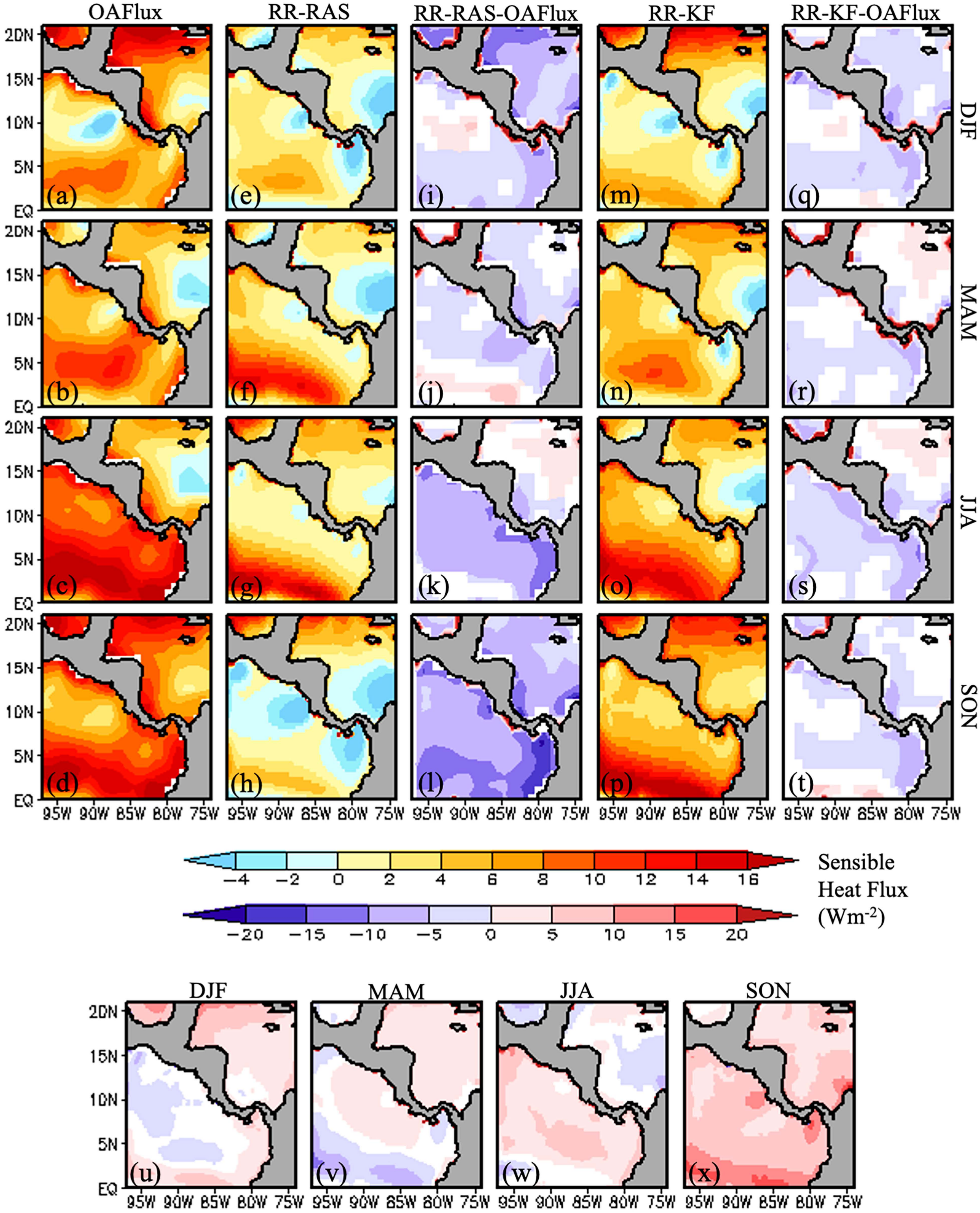

FIG. 7. The seasonal mean climatological surface sensible heat flux (W m^{-2}; shaded) from (a)–(d) observations (OAFlux), (e)–(h) RR-RAS, (i)–(l) systematic errors of RR-RAS, (m)–(p) RR-KF, (q)–(t) systematic errors of RR-KF, and (u)–(x) difference of (RR-KF) − (RR-RAS). The differences are shaded in (u)–(x) only if they exceed the 95% confidence interval.

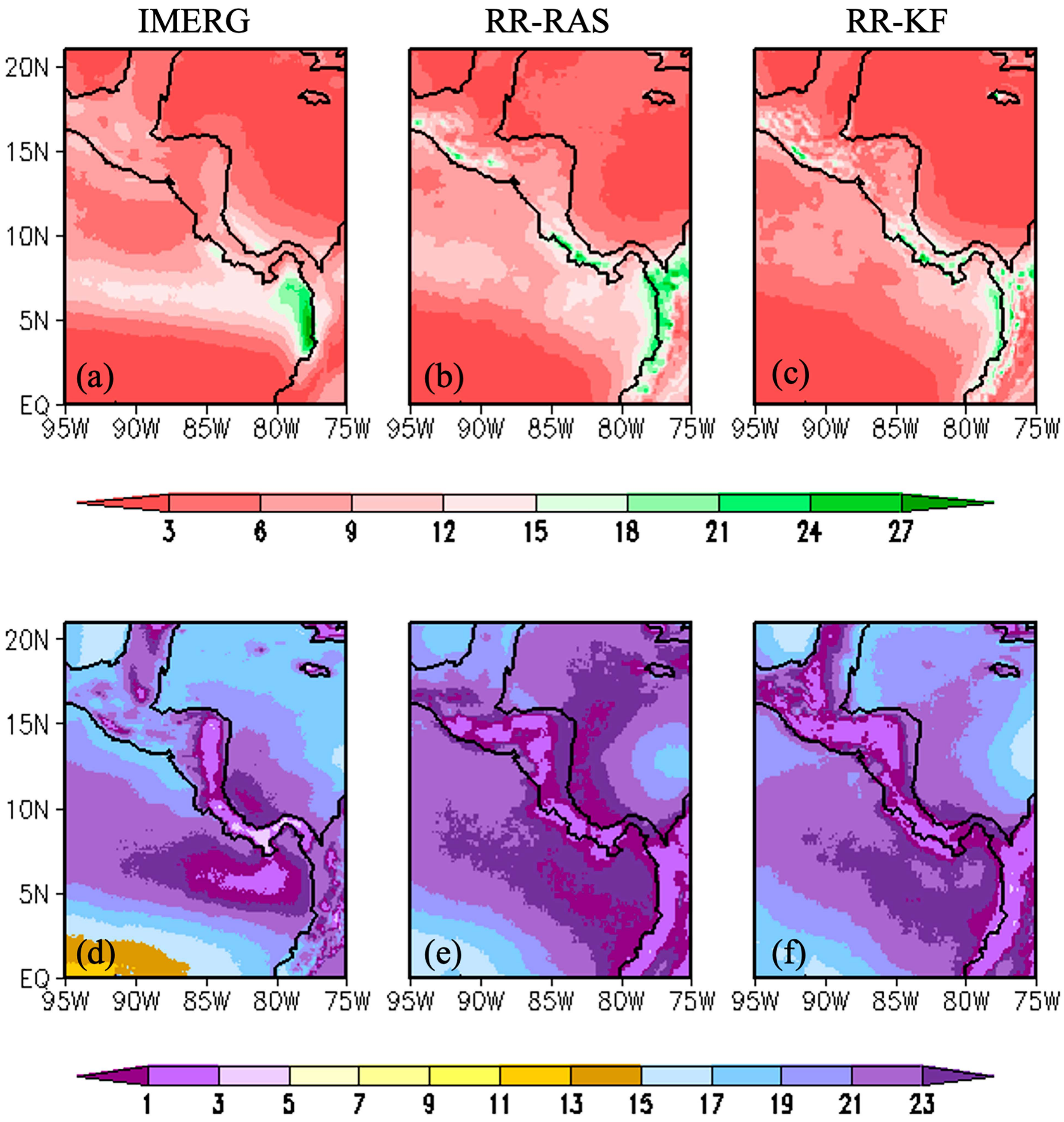

FIG. 8. The mean JJA climatological (a)–(c) diurnal amplitude (mm day^{-1}) and (d)–(f) phase of rainfall (LST) from (a),(d) observations (IMERG), (b),(e) RR-RAS, and (c),(f) RR-KF.

Honduras, El Salvador, and Guatemala and along the coasts of Colombia. The results are very similar for SON (Fig. S8). In both these seasons, however, the differences in the diurnal variations of precipitation between the two models appear relatively small.

c. *Midsummer drought*

The Central American MSD is a well-known phenomenon that relates to the relative minimum of rainfall typically in July and August in between biannual peaks in June and September (Magaña et al. 1999; Taylor and Alfaro 2005). In fact, Gotlieb et al. (2019) indicate that the MSD is most prominent in the Central American dry corridor that is along the Pacific littoral from western Guatemala through northern Costa Rica. The variability in MSD has important agricultural and economic consequences for the region (Hidalgo et al. 2019; Stewart et al. 2022). In Fig. 9, we show the intensity (difference between the average of the biannual peaks of

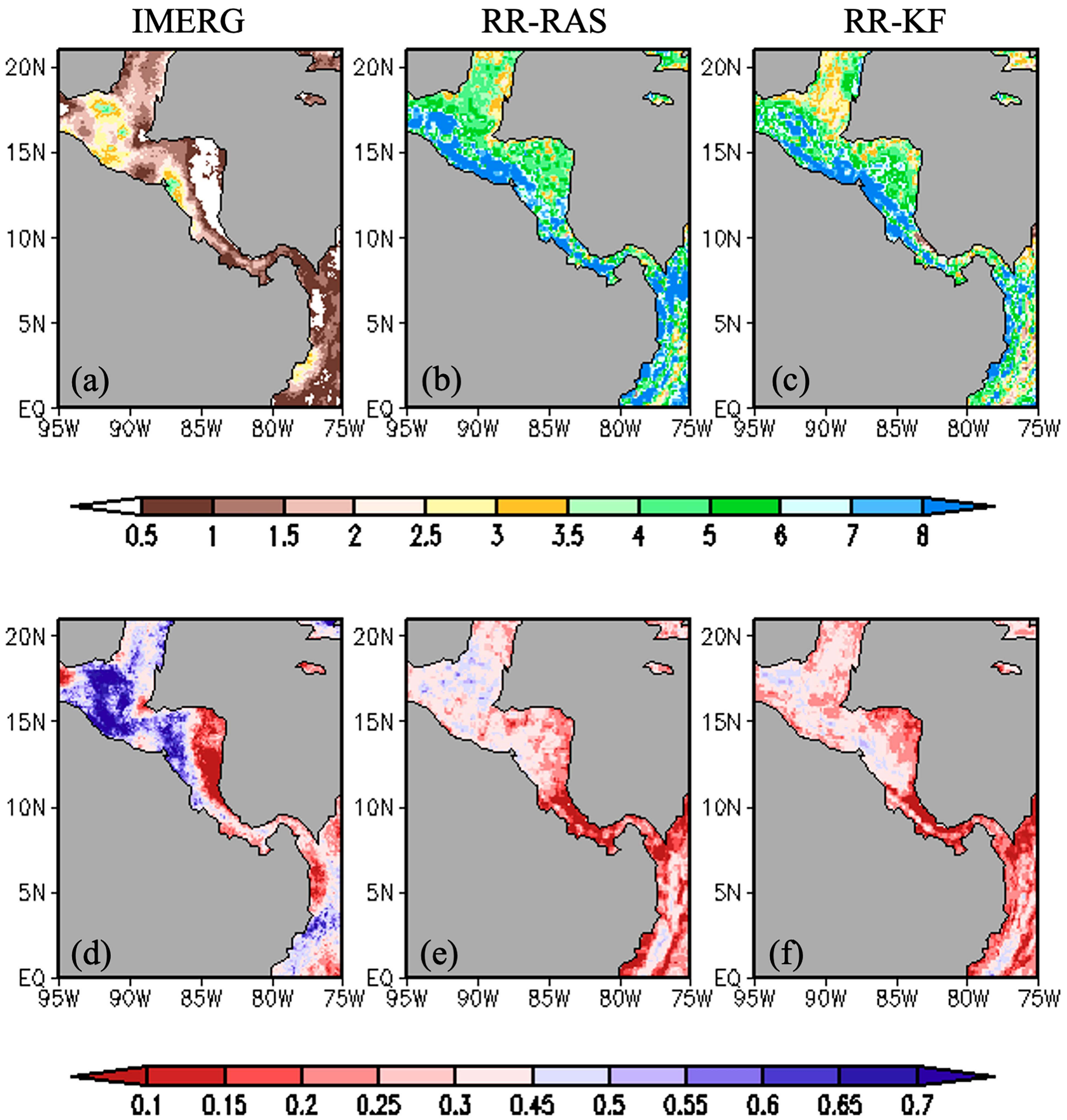

FIG. 9. The (a)–(c) intensity (I; mm day^{-1}) and (d)–(f) frequency (F; fraction of events in 15 years: 1986–2001) of the midsummer drought events from (a),(d) IMERG, (b),(e) RR-RAS, and (c),(f) RR-KF.

rainfall and the average of rainfall in the intervening months between the biannual peaks) and the frequency of its occurrence (as fraction of seasons with MSD in 15 years). As noted earlier, IMERG shows the amplitude of MSD to be largest over the Central American corridor with a relative minimum along the Caribbean coast (Fig. 9a). This pattern is also apparent in the frequency of MSD, with the highest and lowest frequency along the Pacific and Caribbean coasts, respectively. These features are well picked by both models in Figs. 9b, 9c, 9e, and 9f. However, both models overamplify the amplitude of MSD and underestimate the frequency compared to IMERG observations, with the differences between the models appearing insignificant.

5. Discussion

The differences in the simulations of RR–KF and RR–RAS in this study are attributed to changes in the cumulus parameterization scheme as it was the only factor differing in the two regional climate model runs. Both the RAS and the KF schemes are relatively old parameterization schemes developed more than three decades ago. However, they are being compared uniquely in a coupled ocean–atmosphere framework at a relatively higher resolution than most other previous studies over the Central American region.

The concept of the quasi-equilibrium theory adopted in RAS for closure is well interrogated in observations and theory, which over the years has acquired wide acceptance (Emanuel 1994; Raymond and Herman 2011). However, some recent studies have shown that the validity of the quasi-equilibrium assumption is not ubiquitous in the tropics. In convective quasi-equilibrium theory, the subcloud layer and the free troposphere are closely tied in such a way that change in the boundary layer entropy is associated with a corresponding change of equal magnitude in the saturated moist adiabat in the free troposphere to keep the CAPE or the cloud work function in relation to cloud ensemble unchanged (Emanuel 1994). Lin et al. (2015) using radiosonde observations show that the quasi-equilibrium theory is routinely violated in the mid- and upper troposphere of the tropics because of the influence of shallow convection, stratiform precipitation, and convective downdrafts. These processes tend to decouple the free troposphere from the boundary layer. But many cumulus parameterization schemes including RAS treat the full column to be in convective quasi equilibrium, which tends to overestimate the tropospheric heating associated with moist static energy increase in the boundary layer and consequently distort the SST response from associated cloud cover and wind stress changes (Lin et al. 2015). Lin et al. (2015) further note that some of the more recent generation models employing RAS or RAS-type schemes have improved their simulations of convection from their predecessor versions by adding convective triggers that avoid the immediate removal of the environmental instability.

Our study supports some of these observations, given that RR–KF does improve several aspects of the regional climate including the reduction of the terrestrial wet bias, dry bias of the atmospheric column in the oceans, and westerly bias of the low-level trades. Additionally, RR–KF improves the ITCZ location in the eastern Pacific, the simulation of the Choco jet, and the cold bias of the coastal SSTs relative to the RR–RAS simulation. These findings are also consistent with other studies that have compared RAS with KF, which concluded that the latter is superior to the former in simulating convection (e.g., Gallus 1999; Zhang and Wang 2006; Bechtold et al. 2014). However, KF is not a panacea to all the limitations of the climate simulation over the region as is evident from this study as well. For instance, the dry bias over the ITCZ in the eastern Pacific Ocean and the wet bias over the terrestrial regions of the domain are pending issues with the RR–KF simulation. Furthermore, some of these errors could have their origins to lateral boundary conditions of the regional model and/or nonlinear interactions with other parameterization schemes in the regional model.

6. Conclusions

This study examined the differences between two regional climate model (RCM) simulations centered over the Central American region that differed only in their cumulus parameterization schemes. The isthmus of Central America is a challenging geographical area in the deep tropics with steep orography over a narrow terrestrial region surrounded by tropical oceans that display significant variability. The region is known for year-round convective activity with some of the rainiest regions of the world located in the domain. Although earlier studies have been conducted with regional atmospheric models over the region, this work is unique in the fact that we use a regional coupled ocean–atmosphere model to examine the sensitivity to cumulus parameterization scheme. In such a framework, where the ocean and atmosphere are coevolving, the differences in the model simulations between the two cumulus parameterization schemes also reflect the coupled air–sea feedback that is part of the real-world climate variations.

In this study, we tested two commonly used cumulus parameterizations schemes of RAS and KF, which are conceptually different in a coupled ocean–atmosphere model (RSM–ROMS) at a resolution of 15-km grid spacing over a 15-yr integration. RAS is based on quasi-equilibrium theory, where the convection tries to maintain a quasi equilibrium by stabilizing the atmospheric column as it is destabilized by large-scale processes. In KF, a mass flux scheme, convection is triggered when a threshold of CAPE and moisture convergence is reached. The two schemes had a significant impact on the regional climate simulation over Central America forced by the global reanalysis of the atmosphere and the ocean in our coupled RSM–ROMS model. The RR–KF simulation consistently reduces the terrestrial wet bias, enhances the accuracy of the ITCZ location in the eastern Pacific, decreases the dry bias of the atmospheric column over the oceans, mitigates the westerly bias of the low-level trades, refines the simulation of the Choco jet, and reduces the cold bias of coastal SSTs compared to the RR–RAS simulation. In contrast, the diurnal variations in precipitation and the midsummer drought phenomenon were comparable in the two regional model simulations. The diurnal variations of precipitation in the boreal summer and fall seasons in both the simulations had reasonable amplitude and phase in comparison to observations. Similarly, the midsummer drought was reasonable qualitatively with the Caribbean coast showing a smaller amplitude and frequency than the Pacific coast of Central America. However, the model simulations overamplified the biannual peaks of the rainfall compared to the observations.

The overall improvements in the RR–KF simulation relative to RR–RAS are encouraging. There are obviously features in the RR–KF simulation that still require further improvement like the dry bias over the ITCZ in the eastern Pacific Ocean and wet bias over the terrestrial regions of the domain. In a modeling framework with coupled air–sea feedback in regions like Central American, these improvements will likely come incrementally and will require a sustained and systematic approach of testing these schemes in clean sets of twin experiments as attempted here. Nonetheless, this study shows that climate simulations of the oceanic and the atmospheric features of the Central American region stand to benefit in using a mass flux scheme with a convective trigger compared to a quasi-equilibrium-based convection scheme.

Acknowledgments. We acknowledge the support from NASA Grant 80NSSC22K0595.

Data availability statement. The IMERG rainfall from NASA was obtained from NASA (2022). The ERA5 reanalysis data were from ERA5 (https://www.ecmwf.int/en/forecasts/datasets/reanalysis-datasets/era5), the mixed layer depth from Argo was obtained from Holte et al. (2017), and the SODAv2.2.4 ocean reanalysis data were obtained from NOAA (2022). The NCEP-DOE (R2) reanalysis data at 6-hourly interval were obtained from UCAR (2022), or alternatively, the data can also be accessed from PSL (2022). The data from the RSM-ROMS integration to generate the figures in the manuscript will be made available upon request.

REFERENCES

Alfaro, E. J., 2002: Some characteristics of the annual precipitation cycle in central America and their relationship with its surrounding tropical oceans (in Spanish). *Top. Meteor. Oceanogr.*, **9**, 88–103.

——, X. Chourio, A. G. Muñoz, and S. J. Mason, 2018: Improved seasonal prediction skill of rainfall for the primera season in Central America. *Int. J. Climatol.*, **38**, e255–e268, https://doi.org/10.1002/joc.5366.

Almazroui, M., and Coauthors, 2021: Projected changes in temperature and precipitation over the United States, central America, and the Caribbean in CMIP6 GCMs. *Earth Syst. Environ.*, **5**, 1–24, https://doi.org/10.1007/s41748-021-00199-5.

Alpert, J., M. Kanamitsu, P. Caplan, J. Sela, and G. White, 1988: Mountain induced gravity wave drag parameterization in the NMC medium-range forecast model. *Eighth Conf. on Numerical Weather Prediction*, Baltimore, MD, Amer. Meteor. Soc., 726–733.

Amador, J. A., 1998: A climatic feature of the tropical Americas: The trade wind easterly jet. *Top. Meteor. Oceanogr.*, **5**, 91–102.

——, 2008: The intra-Americas sea low-level jet: Overview and future research. *Ann. N. Y. Acad. Sci.*, **1146**, 153–188, https://doi.org/10.1196/annals.1446.012.

——, V. O. Magaña, and J. B. Pérez, 2000: The low level jet and convective activity in the Caribbean. *Proc. 24th Conf. on Hurricanes and Tropical Meteorology*, Fort Lauderdale, FL, Amer. Meteor. Soc., 114–115, https://ams.confex.com/ams/last2000/techprogram/paper_12834.htm.

——, E. J. Alfaro, O. G. Lizano, and V. O. Magaña, 2006: Atmospheric forcing of the eastern tropical Pacific: A review. *Prog. Oceanogr.*, **69**, 101–142, https://doi.org/10.1016/j.pocean.2006.03.007.

Bechtold, P., N. Semane, P. Lopez, J.-P. Chaboureau, A. Beljaars, and N. Bormann, 2014: Representing equilibrium and nonequilibrium convection in large-scale models. *J. Atmos. Sci.*, **71**, 734–753, https://doi.org/10.1175/JAS-D-13-0163.1.

Bhardwaj, A., and V. Misra, 2019: The role of air-sea coupling in the downscaled hydroclimate projection over peninsular Florida and the west Florida shelf. *Climate Dyn.*, **53**, 2931–2947, https://doi.org/10.1007/s00382-019-04669-5.

Brown, A., S. Milton, M. Cullen, B. Golding, J. Mitchell, and A. Shelly, 2012: Unified modeling and prediction of weather and climate: A 25-year journey. *Bull. Amer. Meteor. Soc.*, **93**, 1865–1877, https://doi.org/10.1175/BAMS-D-12-00018.1.

Budakoti, S., C. Singh, and P. K. Pal, 2019: Assessment of various cumulus parameterization schemes for the simulation of very heavy rainfall event based on optimal ensemble approach. *Atmos. Res.*, **218**, 195–206, https://doi.org/10.1016/j.atmosres.2018.12.005.

Cabos, W., and Coauthors, 2019: Dynamical downscaling of historical climate over CORDEX Central America domain with a regionally coupled atmosphere–ocean model. *Climate Dyn.*, **52**, 4305–4328, https://doi.org/10.1007/s00382-018-4381-2.

Carton, J. A., and B. S. Giese, 2008: A reanalysis of ocean climate using Simple Ocean Data Assimilation (SODA). *Mon. Wea. Rev.*, **136**, 2999–3017, https://doi.org/10.1175/2007MWR1978.1.

Cavazos, T., R. Luna-Nino, R. Cerezo-Mota, R. Fuentes-Franco, M. Mendez, L. F. P. Martinez, and E. Valenzuela, 2020: Climatic trends and regional climate models intercomparison over the CORDEX-CAM (Central America, Caribbean, and Mexico) domain. *Int. J. Climatol.*, **40**, 1396–1420, https://doi.org/10.1002/joc.6276.

Charney, J. G., and M. E. Stern, 1962: On the stability of internal baroclinic jets in a rotating atmosphere. *J. Atmos. Sci.*, **19**, 159–172, https://doi.org/10.1175/1520-0469(1962)019<0159:OTSOIB>2.0.CO;2.

Chelton, D. B., M. H. Freilich, and S. K. Esbensen, 2000a: Satellite observations of the wind jets off the Pacific coast of Central America. Part I: Case studies and statistical characteristics. *Mon. Wea. Rev.*, **128**, 1993–2018, https://doi.org/10.1175/1520-0493(2000)128<1993:SOOTWJ>2.0.CO;2.

——, ——, and ——, 2000b: Satellite observations of the wind jets off the Pacific coast of Central America. Part II: Regional relationships and dynamical considerations. *Mon. Wea. Rev.*, **128**, 2019–2043, https://doi.org/10.1175/1520-0493(2000)128<2019:SOOTWJ>2.0.CO;2.

——, and Coauthors, 2001: Observations of coupling between surface wind stress and sea surface temperature in the eastern tropical Pacific. *J. Climate*, **14**, 1479–1498, https://doi.org/10.1175/1520-0442(2001)014<1479:OOCBSW>2.0.CO;2.

Chen, D., A. Dai, and A. Hall, 2021: The convective-to-total precipitation ratio and the "drizzling" bias in climate models. *J. Geophys. Res. Atmos.*, **126**, e2020JD034198, https://doi.org/10.1029/2020JD034198.

Chou, M. D, and M. J. Suarez, 1994: An efficient thermal infrared radiation parameterization for use in general circulation models. NASA Tech. Memo. NASA-TM-104606/Vol. **3**, 98 pp., https://ntrs.nasa.gov/archive/nasa/casi.ntrs.nasa.%20gov/19950009331.pdf.

Chou, M.-D., and K.-T. Lee, 1996: Parameterizations for the absorption of solar radiation by water vapor and ozone. *J. Atmos. Sci.*, **53**, 1203–1208, https://doi.org/10.1175/1520-0469(1996)053<1203:PFTAOS>2.0.CO;2.

Corrales-Suastegui, A., R. Fuentes-Franco, and E. G. Pavia, 2020: The mid-summer drought over Mexico and Central America in the 21st century. *Int. J. Climatol.*, **40**, 1703–1715, https://doi.org/10.1002/joc.6296.

Curtis, S., 2004: Diurnal cycle of rainfall and surface winds and the mid-summer drought of Mexico/Central America. *Climate Res.*, **27** (1), 1–8, https://doi.org/10.3354/cr027001.

Dai, A., and J. Wang, 1999: Diurnal and semidiurnal tides in global surface pressure fields. *J. Atmos. Sci.*, **56**, 3874–3891, https://doi.org/10.1175/1520-0469(1999)056<3874:DASTIG>2.0.CO;2.

Davis, R. E., B. P. Hayden, D. A. Gay, W. L. Phillips, and G. V. Jones, 1997: The North Atlantic subtropical anticyclone. *J. Climate*, **10**, 728–744, https://doi.org/10.1175/1520-0442(1997)010<0728:TNASA>2.0.CO;2.

Diro, G. T., S. A. Rauscher, F. Giorgi, and A. M. Tompkins, 2012: Sensitivity of seasonal climate and diurnal precipitation over Central America to land and sea surface schemes in RegCM4. *Climate Res.*, **52**, 31–48, https://doi.org/10.3354/cr01049.

Durán-Quesada, A. M., L. Gimeno, and J. Amador, 2017: Role of moisture transport for Central American precipitation. *Earth Syst. Dyn.*, **8**, 147–161, https://doi.org/10.5194/esd-8-147-2017.

——, R. Sori, P. Ordonez, and L. Gimeno, 2020: Climate perspectives in the Intra–Americas seas. *Atmosphere*, **11**, 959, https://doi.org/10.3390/atmos11090959.

Ek, M. B., K. E. Mitchell, Y. Lin, E. Rogers, P. Grunmann, V. Koren, G. Gayno, and J. D. Tarpley, 2003: Implementation of Noah land surface model advances in the National Centers for Environmental Prediction operational mesoscale Eta model. *J. Geophys. Res.*, **108**, 8851, https://doi.org/10.1029/2002JD003296.

Emanuel, K. A., 1994: *Atmospheric Convection.* Oxford University Press, 580 pp.

Ezer, T., H. Arango, and A. F. Shchepetkin, 2002: Developments in terrain-following ocean models: Intercomparisons of numerical aspects. *Ocean Modell.*, **4**, 249–267, https://doi.org/10.1016/S1463-5003(02)00003-3.

Feng, Z., and Coauthors, 2025: Mesoscale Convective Systems Tracking Method Intercomparison (MCSMIP): Application to DYAMOND global km-scale simulations. *J. Geophys. Res. Atmos.*, **130**, e2024JD042204, https://doi.org/10.1029/2024JD042204.

Fiedler, P. C., 2002: The annual cycle and biological effects of the Costa Rica dome. *Deep-Sea Res. I*, **49**, 321–338, https://doi.org/10.1016/S0967-0637(01)00057-7.

Gallus, W. A., 1999: Eta simulations of three extreme precipitation events: Sensitivity to resolution and convective parameterization. *Wea. Forecasting*, **14**, 405–426, https://doi.org/10.1175/1520-0434(1999)014<0405:ESOTEP>2.0.CO;2.

Garreaud, R., and J. M. Wallace, 1997: The diurnal march of convective cloudiness over the Americas. *Mon. Wea. Rev.*, **125**, 3157–3171, https://doi.org/10.1175/1520-0493(1997)125<3157:TDMOCC>2.0.CO;2.

Giannini, A., Y. Kushnir, and M. A. Cane, 2000: Interannual variability of Caribbean rainfall, ENSO, and the Atlantic Ocean. *J. Climate*, **13**, 297–311, https://doi.org/10.1175/1520-0442(2000)013<0297:IVOCRE>2.0.CO;2.

Giorgi, F., 2006: Climate change hot-spots. *Geophys. Res. Lett.*, **33**, L08707, https://doi.org/10.1029/2006GL025734.

Glazer, R. H., and V. Misra, 2018: Ice versus liquid water saturation in simulations of the Indian summer monsoon. *Climate Dyn.*, **51**, 3847–3863, https://doi.org/10.1007/s00382-018-4116-4.

Gotlieb, Y., P. Pérez-Briceño, H. Hidalgo, and E. Alfaro, 2019: The Central American Dry Corridor: A consensus statement and its background. *Rev. Yu'am*, **3**, 42–51.

Haidvogel, D. B., H. G. Arango, K. Hedstrom, A. Beckmann, P. Malanotte-Rizzoli, and A. F. Shchepetkin, 2000: Model evaluation experiments in the North Atlantic basin: Simulations in nonlinear terrain-following coordinates. *Dyn. Atmos. Oceans*, **32**, 239–281, https://doi.org/10.1016/S0377-0265(00)00049-X.

Ham, S., K. Yoshimura, and H. Li, 2016: Historical dynamical downscaling for East Asia with the atmosphere and ocean coupled regional model. *J. Meteor. Soc. Japan*, **94A**, 199–208, https://doi.org/10.2151/jmsj.2015-046.

Hamilton, H. L., G. S. Young, J. L. Evans, J. D. Fuentes, and K. M. Núñez Ocasio, 2017: The relationship between the Guinea Highlands and the West African offshore rainfall maximum. *Geophys. Res. Lett.*, **44**, 1158–1166, https://doi.org/10.1002/2016GL071170.

——, K. M. Núñez Ocasio, J. L. Evans, G. S. Young, and J. D. Fuentes, 2020: Topographic influence on the African easterly jet and African easterly wave energetics. *J. Geophys. Res. Atmos.*, **125**, e2019JD03213, https://doi.org/10.1029/2019JD032138.

Hastenrath, S., and D. Polzin, 2013: Climatic variations in Central America and the Caribbean. *Int. J. Climatol.*, **33**, 1348–1356, https://doi.org/10.1002/joc.3515.

Hersbach, H., and Coauthors, 2019: The ERA5 global reanalysis. *Quart. J. Roy. Meteor. Soc.*, **146**, 1999–2049, https://doi.org/10.1002/qj.3803.

Hidalgo, H. G., and E. J. Alfaro, 2015: Skill of CMIP5 climate models in reproducing 20th century basic climate features in Central America. *Int. J. Climatol.*, **35**, 3397–3421, https://doi.org/10.1002/joc.4216.

——, A. M. Durán-quesada, J. A. Amador, and E. J. Alfaro, 2015: The Caribbean low-level jet, the inter-tropical convergence zone and precipitation patterns in the Intra-Americas Sea: A proposed dynamical mechanism. *Geogr. Ann.*, **97A**, 41–59, https://doi.org/10.1111/geoa.12085.

——, E. J. Alfaro, J. A. Amador, and Á. Bastidas, 2019: Precursors of quasi-decadal dry-spells in the Central America Dry Corridor. *Climate Dyn.*, **53**, 1307–1322, https://doi.org/10.1007/s00382-019-04638-y.

——, ——, F. Hernãandez-Castro, and P. M. Pérez-Briceño, 2020: Identification of tropical cyclones' critical positions associated with extreme precipitation events in Central America. *Atmosphere*, **11**, 1123, https://doi.org/10.3390/atmos11101123.

Holbach, H. M., and M. A. Bourassa, 2014: The effects of gap-wind-induced vorticity, the monsoon trough, and the ITCZ on East Pacific tropical cyclogenesis. *Mon. Wea. Rev.*, **142**, 1312–1325, https://doi.org/10.1175/MWR-D-13-00218.1.

Holte, J., L. D. Talley, J. Gilson, and D. Roemmich, 2017: An Argo mixed layer climatology and database. *Geophys. Res. Lett.*, **44**, 5618–5626, https://doi.org/10.1002/2017GL073426.

Hong, S.-Y., and H.-L. Pan, 1996: Nonlocal boundary layer vertical diffusion in a Medium-Range Forecast Model. *Mon. Wea. Rev.*, **124**, 2322–2339, https://doi.org/10.1175/1520-0493(1996)124<2322:NBLVDI>2.0.CO;2.

Huffman, G. J., and Coauthors, 2023: NASA Global Precipitation Measurement (GPM) Integrated Multi-satellitE Retrievals for GPM (IMERG). Algorithm Theoretical Basis Doc., version 07, 52 pp., https://gpm.nasa.gov/sites/default/files/2023-07/IMERG_V07_ATBD_final_230712.pdf.

——, and Coauthors, 2024: IMERG V07 release notes. PPS, 23 pp., https://gpm.nasa.gov/resources/documents/imerg-v07-release-notes.

Jenney, A. M., R. A. Houze Jr., M. LeMone, E. J. Thompson, K. M. Núñez Ocasio, C. Zhang, and T. R. Nathan, 2025: Celebrating 50 years since GATE. *Bull. Amer. Meteor. Soc.*, **106**, E576–E595, https://doi.org/10.1175/BAMS-D-24-0063.1.

Juang, H. H., and M. Kanamitsu, 1994: The NMC nested regional spectral model. *Mon. Wea. Rev.*, **122**, 3–26, https://doi.org/10.1175/1520-0493(1994)122<0003:TNNRSM>2.0.CO;2.

Kain, J. S., 2004: The Kain–Fritsch convective parameterization: An update. *J. Appl. Meteor.*, **43**, 170–181, https://doi.org/10.1175/1520-0450(2004)043<0170:TKCPAU>2.0.CO;2.

——, and M. Fritsch, 1993: Convective parameterization for mesoscale models: The Kain-Fritsch scheme. *The Representation of Cumulus Convection in Numerical Models*, *Meteor. Monogr.*, No. 24, Amer. Meteor. Soc., 165–170, https://doi.org/10.1007/978-1-935704-13-3_16.

Kanamitsu, M., W. Ebusuzaki, J. Woollen, S.-K. Yang, J. Hnilo, M. Fiorino, and G. L. Potter II, 2002: NCEP–DOE AMIP-II reanalysis (R-2). *Bull. Amer. Meteor. Soc.*, **83**, 1631–1644, https://doi.org/10.1175/BAMS-83-11-1631.

——, K. Yoshimura, B. Y. Yhang, and S. Y. Hong, 2010: Errors of interannual variability and trend in dynamical downscaling of reanalysis. *J. Geophys. Res.*, **115**, D17115, https://doi.org/10.1029/2009JD013511.

Karmalkar, A. V., R. S. Bradley, and H. F. Diaz, 2011: Climate change in Central America and Mexico: Regional climate model validation and climate change projections. *Climate Dyn.*, **37**, 605–629, https://doi.org/10.1007/s00382-011-1099-9.

Kowal, K. M., L. J. Slater, A. G. Lopez, and A. F. Van Loon, 2023: A comparison of seasonal rainfall forecasts over Central America using dynamic and hybrid approaches from Copernicus Climate Change Service seasonal forecasting system and the North American Multimodel Ensemble. *Int. J. Climatol.*, **43**, 2175–2199, https://doi.org/10.1002/joc.7969.

Large, W. G., J. C. McWilliams, and S. C. Doney, 1994: Oceanic vertical mixing: A review and a model with a nonlocal boundary layer parameterization. *Rev. Geophys.*, **32**, 363–403, https://doi.org/10.1029/94RG01872.

Li, H., and V. Misra, 2014: Thirty-two-year ocean–atmosphere coupled downscaling of global reanalysis over the Intra-American Seas. *Climate Dyn.*, **43**, 2471–2489, https://doi.org/10.1007/s00382-014-2069-9.

——, M. Kanamitsu, S.-Y. Hong, K. Yoshimura, D. R. Cayan, and V. Misra, 2014: A high-resolution ocean-atmosphere coupled downscaling of the present climate over California. *Climate Dyn.*, **42**, 701–714, https://doi.org/10.1007/s00382-013-1670-7.

Lin, J., T. Qian, T. Shinoda, and S. Li, 2015: Is the tropical atmosphere in convective quasi-equilibrium? *J. Climate*, **28**, 4357–4372, https://doi.org/10.1175/JCLI-D-14-00681.1.

Magaña, V., J. A. Amador, and S. Medina, 1999: The midsummer drought over Mexico and Central America. *J. Climate*, **12**, 1577–1588, https://doi.org/10.1175/1520-0442(1999)012<1577:TMDOMA>2.0.CO;2.

Maldonado, T., E. J. Alfaro, and H. G. Hidalgo, 2018: A review of the main drivers and variability of Central America's climate and seasonal forecast systems. *Rev. Biol. Trop.*, **66**, 153–175, https://doi.org/10.15517/rbt.v66i1.33294.

Mapes, B. E., T. T. Warner, M. Xu, and A. J. Negri, 2003a: Diurnal patterns of rainfall in northwestern South America. Part I: Observations and context. *Mon. Wea. Rev.*, **131**, 799–812, https://doi.org/10.1175/1520-0493(2003)131<0799:DPORIN>2.0.CO;2.

——, ——, and ——, 2003b: Diurnal patterns of rainfall in northwestern South America. Part III: Diurnal gravity waves and nocturnal convection offshore. *Mon. Wea. Rev.*, **131**, 830–844, https://doi.org/10.1175/1520-0493(2003)131<0830:DPORIN>2.0.CO;2.

——, ——, ——, and D. J. Gochis, 2004: Comparison of cumulus parameterizations and entrainment using domain-mean wind divergence in a regional model. *J. Climate*, **61**, 1284–1295, https://doi.org/10.1175/1520-0469(2004)061<1284:COCPAE>2.0.CO;2.

Martinez, C., L. Goddard, Y. Kushnir, and M. Ting, 2019: Seasonal climatology and dynamical mechanisms of rainfall in the Caribbean. *Climate Dyn.*, **53**, 825–846, https://doi.org/10.1007/s00382-019-04616-4.

Martínez-Castro, D., A. Vichot-Llano, A. Bezanilla-Morlot, A. Centella-Artola, J. Campbell, F. Giorgi, and C. C. Viloria-Holguin, 2018: The performance of RegCM4 over the Central America and Caribbean region using different cumulus parameterizations. *Climate Dyn.*, **50**, 4103–4126, https://doi.org/10.1007/s00382-017-3863-y.

Mellor, G. L., and T. Yamada, 1982: Development of a turbulence closure model for geophysical fluid problems. *Rev. Geophys.*, **20**, 851–875, https://doi.org/10.1029/RG020i004p00851.

Misra, V., and L. Marx, 2007: Manifestation of remote response over the equatorial Pacific in a climate model. *J. Geophys. Res.*, **112**, D20105, https://doi.org/10.1029/2007JD008597.

——, and C. B. Jayasankar, 2022: A high resolution coupled ocean-atmosphere simulation of the regional climate over Central America. *Climate Dyn.*, **58**, 2981–3001, https://doi.org/10.1007/s00382-021-06083-2.

——, and ——, 2025: The regional coupled ocean-atmosphere model simulation over eastern tropical Africa. *Dyn. Atmos. Oceans*, **109**, 101520, https://doi.org/10.1016/j.dynatmoce.2024.101520.

——, H. Li, and M. Kozar, 2014: The precursors in the Intra-Americas seas to seasonal climate variations over North America. *J. Geophys. Res. Oceans*, **119**, 2938–2948, https://doi.org/10.1002/2014JC009911.

——, A. Mishra, and A. Bhardwaj, 2018: Simulation of the intraseasonal variations of the Indian summer monsoon in a regional coupled ocean–atmosphere model. *J. Climate*, **31**, 3167–3185, https://doi.org/10.1175/JCLI-D-17-0434.1.

Molinari, J., D. Knight, M. Dickinson, D. Vollaro, and S. Skubis, 1997: Potential vorticity, easterly waves, and eastern Pacific tropical cyclogenesis. *Mon. Wea. Rev.*, **125**, 2699–2708, https://doi.org/10.1175/1520-0493(1997)125<2699:PVEWAE>2.0.CO;2.

Moorthi, S., and M. J. Suarez, 1992: Relaxed Arakawa-Schubert. A parameterization of moist convection for general circulation models. *Mon. Wea. Rev.*, **120**, 978–1002, https://doi.org/10.1175/1520-0493(1992)120<0978:RASAPO>2.0.CO;2.

Mora, G., 2017: Climatology of the low-level winds over the Intra-Americas sea using satellite and reanalysis data. 17 pp., https://www.researchgate.net/profile/Gabriela-Mora-7/publication/325766427_Climatology_of_the_low-level_winds_over_the_intraamericas_sea_using_satellite_and_reanalysis_data/links/5b22a8f4458515270fcb6413/Climatology-of-the-low-level-winds-over-the-intraamericas-sea-using-satellite-and-reanalysis-data.pdf.

Muñoz, E., A. J. Busalachi, S. Nigam, and A. Ruiz-Barradas, 2008: Winter and summer structure of the Caribbean low-level jet. *J. Climate*, **21**, 1260–1276, https://doi.org/10.1175/2007JCLI1855.1.

Myers, N., R. A. Mittermeier, C. G. Mittermeier, G. A. B. da Fonseca, and J. Kent, 2000: Biodiversity hotspots for conservation priorities. *Nature*, **403**, 853–858, https://doi.org/10.1038/35002501.

NASA, 2022: IMERG V07. Accessed 22 January 2022, https://gpm.nasa.gov/taxonomy/term/1417.

NOAA, 2022: SODA - POP 2.2.4 Monthly Means, 1871-2010 (At Depths). Accessed 23 April 2022, https://catalog.data.gov/dataset/soda-pop-2-2-4-monthly-means-1871-2010-at-depths.

Núñez Ocasio, K. M., J. L. Evans, and G. S. Young, 2020a: Tracking mesoscale convective systems that are potential candidates for tropical cyclogenesis. *Mon. Wea. Rev.*, **148**, 655–669, https://doi.org/10.1175/MWR-D-19-0070.1.

——, ——, and ——, 2020b: A wave-relative framework analysis of AEW–MCS interactions leading to tropical cyclogenesis. *Mon. Wea. Rev.*, **148**, 4657–4671, https://doi.org/10.1175/MWR-D-20-0152.1.

——, A. Brammer, J. L. Evans, G. S. Young, and Z. L. Moon, 2021: Favorable monsoon environment over eastern Africa for subsequent tropical cyclogenesis of African easterly waves. *J. Atmos. Sci.*, **78**, 2911–2925, https://doi.org/10.1175/JAS-D-20-0339.1.

Poveda, G., and O. Mesa, 2000: On the existence of Lloró (the rainiest locality on Earth): Enhanced ocean-land-atmosphere interaction by a low-level jet. *Geophys. Res. Lett.*, **27**, 1675–1678, https://doi.org/10.1029/1999GL006091.

Prein, A. F., P. A. Mooney, and J. M. Done, 2024: Km-scale simulations of mesoscale convective systems over South America—A feature tracker intercomparison. *J. Geophys. Res. Atmos.*, **129**, e2023JD040254, https://doi.org/10.1029/2023JD040254.

PSL, 2022: NCEP/DOE Reanalysis II. NASA, accessed 12 August 2022, https://psl.noaa.gov/data/gridded/data.ncep.reanalysis2.html.

Rajasree, V. P. M., and Coauthors, 2023: Tropical cyclogenesis: Controlling factors and physical mechanisms. *Trop. Cyclone Res. Rev.*, **12**, 165–181, https://doi.org/10.1016/j.tcrr.2023.09.004.

Raymond, D. J., and M. J. Herman, 2011: Convective quasi-equilibrium reconsidered. *J. Adv. Model. Earth Syst.*, **3**, M08003, https://doi.org/10.1029/2011MS000079.

Reynolds, R. W., T. M. Smith, C. Liu, D. B. Chelton, K. S. Casey, and M. G. Schlax, 2007: Daily high-resolution-blended analyses for sea surface temperature. *J. Climate*, **20**, 5473–5496, https://doi.org/10.1175/2007JCLI1824.1.

Rivera, E. R., J. A. Amador, and F. Sáenz, 2022: Sensitivity of precipitation and atmospheric low-level circulation patterns to domain size and choice of parameterization schemes in RegCM4.4 over Central America. *Climate Res.*, **89**, 61–83, https://doi.org/10.3354/cr01707.

Rodgers, J., V. Misra, and C. B. Jayasankar, 2024: Using the observed variations of the start date of the rainy season over Central America for its reliable seasonal outlook. *J. Climate*, **37**, 4901–4913, https://doi.org/10.1175/JCLI-D-23-0699.1.

Rojas, M., and A. Seth, 2003: Simulation and sensitivity in a nested modeling system for Central America. Part I: Control climate. *J. Climate*, **16**, 3684–3701, https://doi.org/10.1175/1520-0442(2003)016<3684:SASIAN>2.0.CO;2.

Romero-Centeno, R., J. Zavala-Hidalgo, A. Gallegos, and J. J. O'Brien, 2003: Isthmus of Tehuantepec wind climatology and ENSO signal. *J. Climate*, **16**, 2628–2639, https://doi.org/10.1175/1520-0442(2003)016<2628:IOTWCA>2.0.CO;2.

——, ——, and G. B. Raga, 2007: Midsummer gap winds and low-level circulation over the eastern tropical Pacific. *J. Climate*, **20**, 3768–3784, https://doi.org/10.1175/JCLI4220.1.

Sáenz, F., H. G. Hidalgo, Á. G. Muñoz, E. J. Alfaro, J. A. Amador, and J. L. Vázquez-Aguirre, 2023: Atmospheric circulation types controlling rainfall in the Central American Isthmus. *Int. J. Climatol.*, **43**, 197–218, https://doi.org/10.1002/joc.7745.

Selman, C., and V. Misra, 2015: Simulating diurnal variations over the southeastern United States. *J. Geophys. Res. Atmos.*, **120**, 180–198, https://doi.org/10.1002/2014JD021812.

Shapiro, M., and Coauthors, 2010: An Earth-system prediction initiative for the twenty-first century. *Bull. Amer. Meteor. Soc.*, **91**, 1377–1388, https://doi.org/10.1175/2010BAMS2944.1.

Shchepetkin, A. F., and J. C. McWilliams, 2005: The Regional Oceanic Modeling System (ROMS): A split-explicit, free-surface, topography-following-coordinate oceanic model. *Ocean Modell.*, **9**, 347–404, https://doi.org/10.1016/j.ocemod.2004.08.002.

Shige, S., Y. Nakano, and M. K. Yamamoto, 2017: Role of orography, diurnal cycle, and intraseasonal oscillation in summer monsoon rainfall over the Western Ghats and Myanmar Coast. *J. Climate*, **30**, 9365–9381, https://doi.org/10.1175/JCLI-D-16-0858.1.

Slingo, J. M., 1987: The development and verification of a cloud prediction scheme for the ECMWF model. *Quart. J. Roy. Meteor. Soc.*, **113**, 899–927, https://doi.org/10.1002/qj.49711347710.

Stewart, I. T., E. P. Maurer, K. Stahl, and K. Joseph, 2022: Recent evidence for warmer and drier growing seasons in climate sensitive regions of Central America from multiple global datasets. *Int. J. Climatol.*, **42**, 1399–1417, https://doi.org/10.1002/joc.7310.

Sundqvist, H., E. Berge, and J. E. Kristjánsson, 1989: Condensation and cloud parameterization studies with a mesoscale numerical weather prediction model. *Mon. Wea. Rev.*, **117**, 1641–1657, https://doi.org/10.1175/1520-0493(1989)117<1641:CACPSW>2.0.CO;2.

Tatsumi, Y., 1986: A spectral limited-area model with time-dependent lateral boundary conditions and its application to a multi-level primitive equation model. *J. Meteor. Soc. Japan*, **64**, 637–664, https://doi.org/10.2151/jmsj1965.64.5_637.

Taylor, M. A., and E. Alfaro, 2005: Climate of Central America and the Caribbean. *Encyclopedia of World Climatology*, J. E. Oliver, Ed., Springer, 183–189.

Tiedtke, M., 1983: The sensitivity of the time-mean large-scale flow to cumulus convection in the ECMWF model. *Proc. ECMWF Workshop on Convective in Large-scale Models*, Reading, United Kingdom, ECMWF, 297–316, https://www.ecmwf.int/en/elibrary/76694-sensitivity-time-mean-large-scale-flow-cumulus-convection-ecmwf-model.

Torres-Alavez, J. A., and Coauthors, 2021: Future projections in the climatology of global low-level jets from CORDEX-CORE simulations. *Climate Dyn.*, **57**, 1551–1569, https://doi.org/10.1007/s00382-021-05671-6.

UCAR, 2022: NCEP/DOE Reanalysis 2 (R2). Accessed 2 December 2022, https://rda.ucar.edu/datasets/ds091.0/.

Umlauf, L., and H. Burchard, 2003: A generic length-scale equation for geophysical turbulence models. *J. Mar. Res.*, **61**, 235–265, https://doi.org/10.1357/002224003322005087.

Velasco, I., and M. Fritsch, 1987: Mesoscale convective complexes in the Americas. *J. Geophys. Res.*, **92**, 9591–9613, https://doi.org/10.1029/JD092iD08p09591.

Vera, C., and Coauthors, 2006: Toward a unified view of the American monsoon systems. *J. Climate*, **19**, 4977–5000, https://doi.org/10.1175/JCLI3896.1.

Wang, C., 2007: Variability of the Caribbean Low-Level Jet and its relations to climate. *Climate Dyn.*, **29**, 411–422, https://doi.org/10.1007/s00382-007-0243-z.

——, and D. B. Enfield, 2001: The tropical Western Hemisphere warm pool. *Geophys. Res. Lett.*, **28**, 1635–1638, https://doi.org/10.1029/2000GL011763.

——, and S.-K. Lee, 2007: Atlantic warm pool, Caribbean low-level jet, and their potential impact on Atlantic hurricanes.

Geophys. Res. Lett., **34**, L02703, https://doi.org/10.1029/2006GL028579.

Whitaker, J. W., and E. D. Maloney, 2020: Genesis of an East Pacific easterly wave from a Panama Bight MCS: A case study analysis from June 2012. *J. Atmos. Sci.*, **77**, 3567–3584, https://doi.org/10.1175/JAS-D-20-0032.1.

Xie, S.-P., H. Xu, W. S. Kessler, and M. Nonaka, 2005: Air–sea interaction over the eastern Pacific warm pool: Gap winds, thermocline dome, and atmospheric convection. *J. Climate*, **18**, 5–20, https://doi.org/10.1175/JCLI-3249.1.

Yang, G., and J. Slingo, 2001: The diurnal cycle in the tropics. *Mon. Wea. Rev.*, **129**, 784–801, https://doi.org/10.1175/1520-0493(2001)129<0784:TDCITT>2.0.CO;2.

Yang, Y.-M., and B. Wang, 2019: Improving MJO simulation by enhancing the interaction between boundary layer convergence and lower tropospheric heating. *Climate Dyn.*, **52**, 4671–4693, https://doi.org/10.1007/s00382-018-4407-9.

Yepes, J., G. Poveda, J. F. Mejia, L. Moreno, and C. Rueda, 2019: Choco-JEX: A research experiment focused on the Chocó low-level jet over the far eastern Pacific and western Colombia. *Bull Amer. Meteor. Soc.*, **100**, 779–796, https://doi.org/10.1175/BAMS-D-18-0045.1.

Yu, L., X. Jin, and R. A. Weller, 2008: Multidecade global flux datasets from the Objectively analyzed Air-sea Fluxes (OAFlux) Project: Latent and sensible heat fluxes, ocean evaporation, and related surface meteorological variables. OAFlux Project Tech. Rep. OA-2008-01, Woods Hole Oceanographic Institution, 64 pp.

Zhang, G. J., and H. Wang, 2006: Toward mitigating the double ITCZ problem in NCAR CCSM3. *Geophys. Res. Lett.*, **33**, L06709, https://doi.org/10.1029/2005GL025229.

Zhao, Q., and F. H. Carr, 1997: A prognostic cloud scheme for operational NWP models. *Mon. Wea. Rev.*, **125**, 1931–1953, https://doi.org/10.1175/1520-0493(1997)125<1931:APCSFO>2.0.CO;2.

Supplemental Material

Journal of Applied Meteorology and Climatology
The Impact of Cumulus Parameterization on Regional Climate Simulations of Central American Climate
https://doi.org/10.1175/JAMC-D-24-0240.1

Supplementary Material

The Impact of Cumulus Parameterization on Regional Climate Simulation of Central American Climate

Justin Gonzalez[1, 2], Vasubandhu Misra[1, 2, #] and C. B. Jayasankar[2]

[1]Department of Earth, Ocean and Atmospheric Science, Florida State University, Tallahassee, Florida, U.S.A.

[2]Center for Ocean-Atmospheric Prediction Studies, Florida State University, Tallahassee, Florida, U.S.A.

Corresponding Author Email: vmisra@fsu.edu

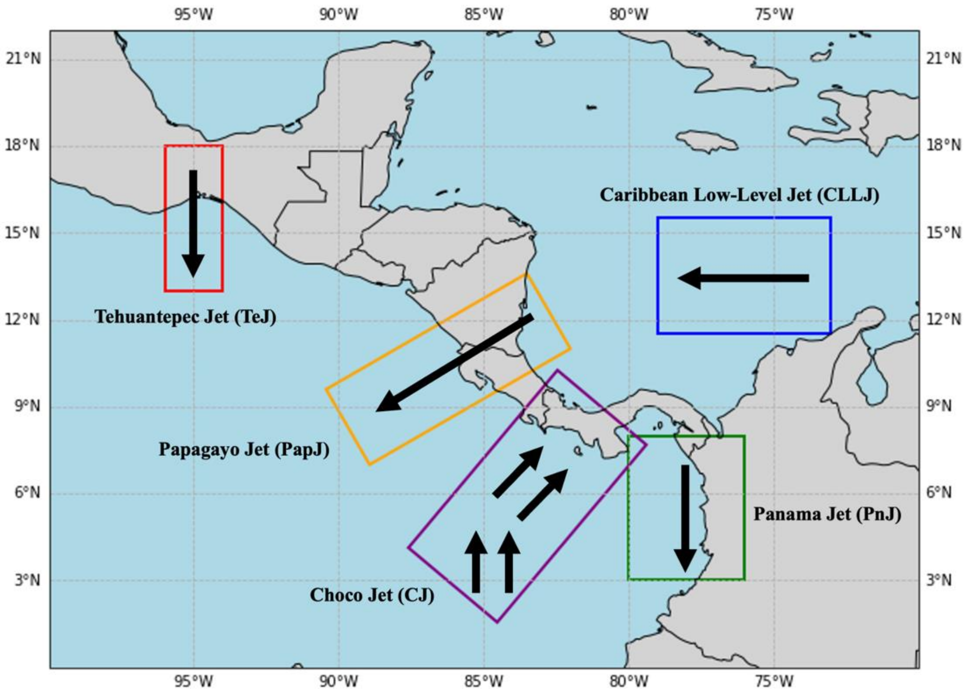

Figure S1: A schematic showing the location and direction of the various low level jets in the region.

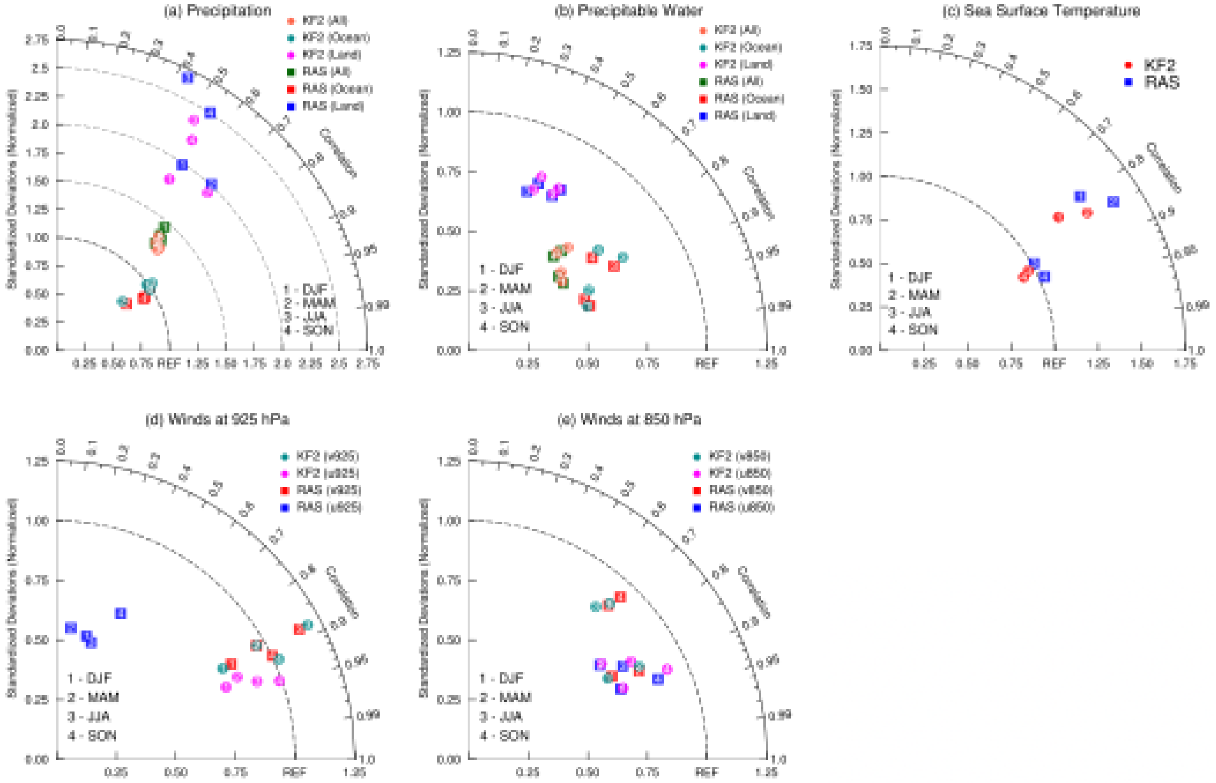

Figure S2: Taylor diagram corresponding to a) Fig. 1 (surface precipitation), b) Fig. 2 (precipitable water), c) Fig. 3 (SST), d) Fig. 4 (925 hPa winds in the main text, and e) Fig. S7 (850 hPa winds) in the supplementary material, . In panel (c) only ocean points are considered. In panels (d) and (e) all land and ocean points in the domain are considered together. The values of the pattern correlation coefficient along the arc and the ratio of the standardized variances of the model to observations along the x-and y-axes are plotted in the Taylor diagram for all points (All), for all land points only (Land) and for all ocean points only (Ocean) in the domain.

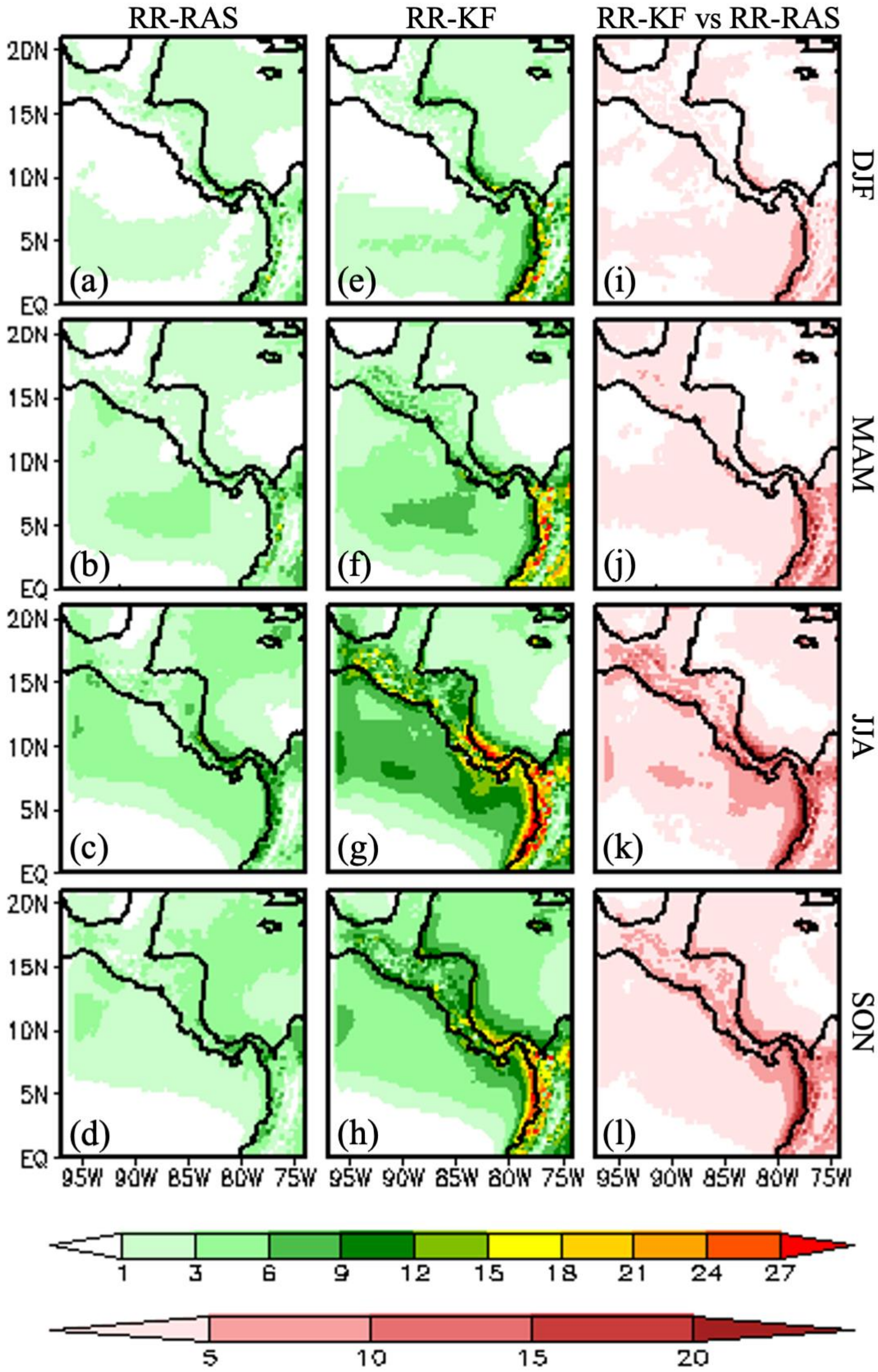

Figure S3: Figure 5: The seasonal mean climatological convective precipitation (mm/day; shaded) from (a, b, c, d) RR-RAS and (e, f, g, h) RR-KF2, and (i, j, k, l) difference of (RR-KF2) – (RR-RAS). The differences are shaded in (i, j, k, l) only if they exceed 95% confidence interval.

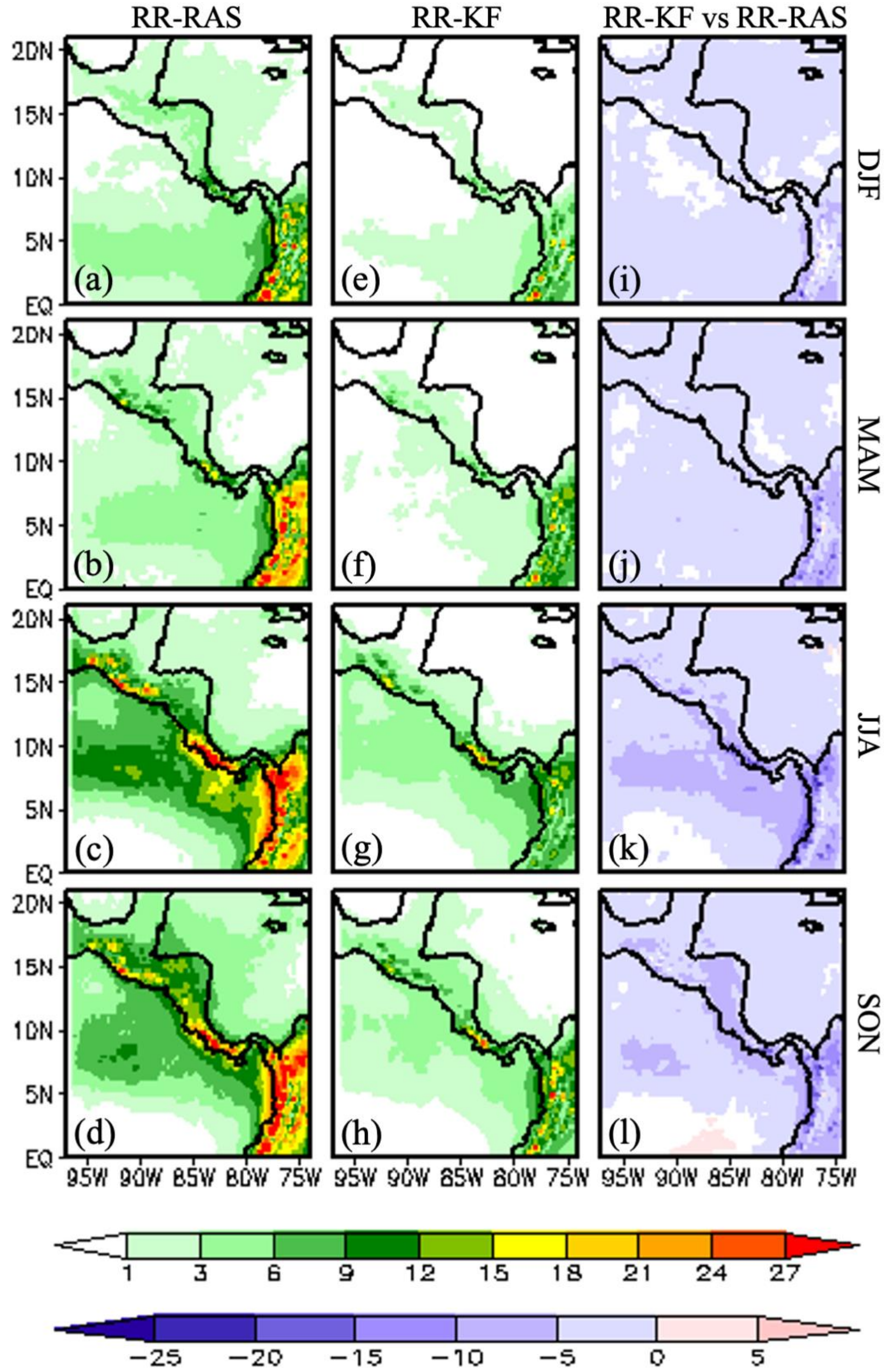

Figure S4: The seasonal mean climatological stratiform precipitation (mm/day; shaded) from (a, b, c, d) RR-RAS and (e, f, g, h) RR-KF2, and (i, j, k, l) difference of (RR-KF2) – (RR-RAS). The differences are shaded in (i, j, k, l) only if they exceed 95% confidence interval.

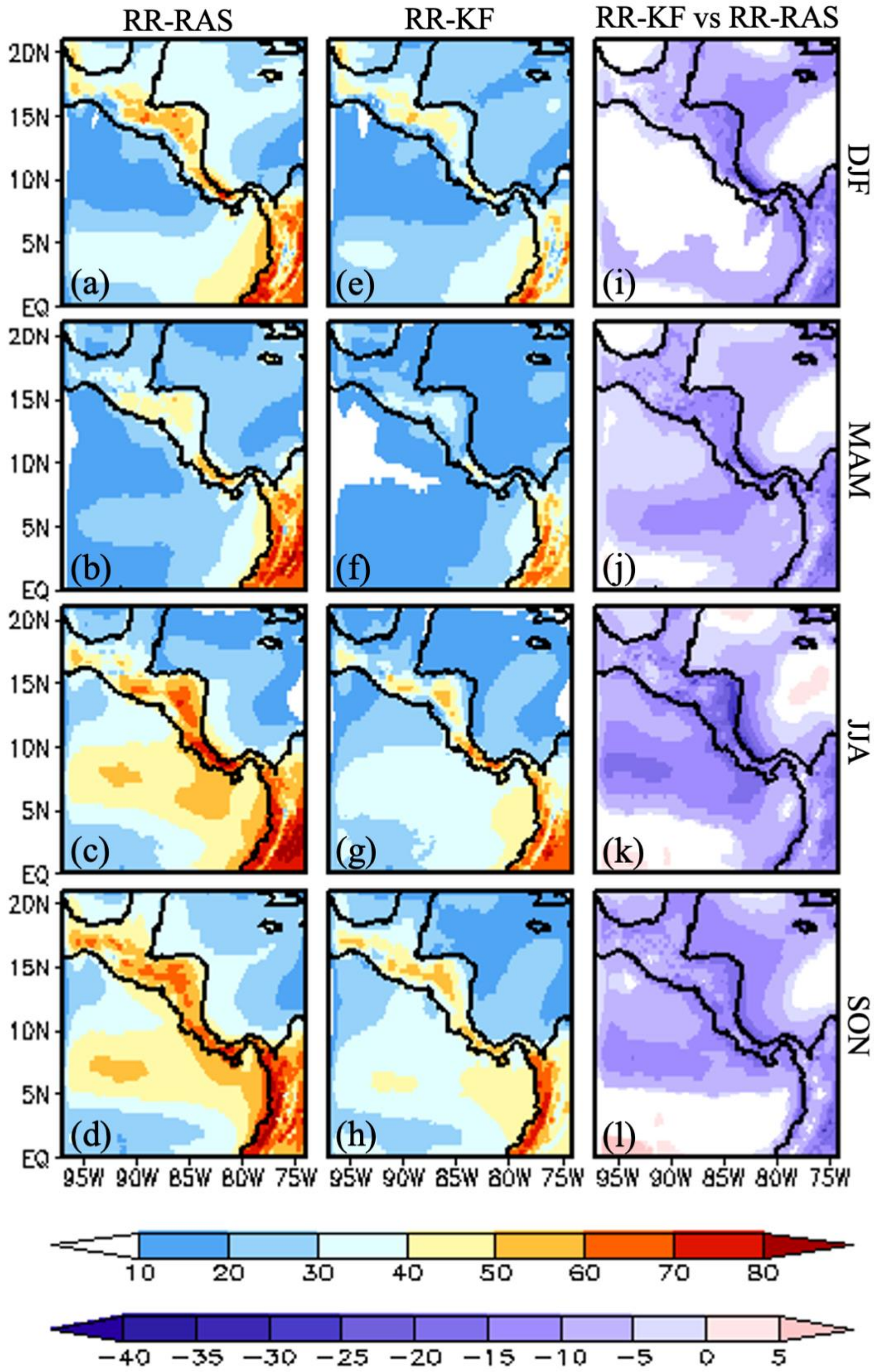

Figure S5: The seasonal mean climatological low-level cloud cover (%; shaded) from (a, b, c, d) RR-RAS and (e, f, g, h) RR-KF2, and (i, j, k, l) corresponding difference of (RR-KF2) – (RR-RAS). The differences are shaded in (i, j, k, l) only if they exceed 95% confidence interval.

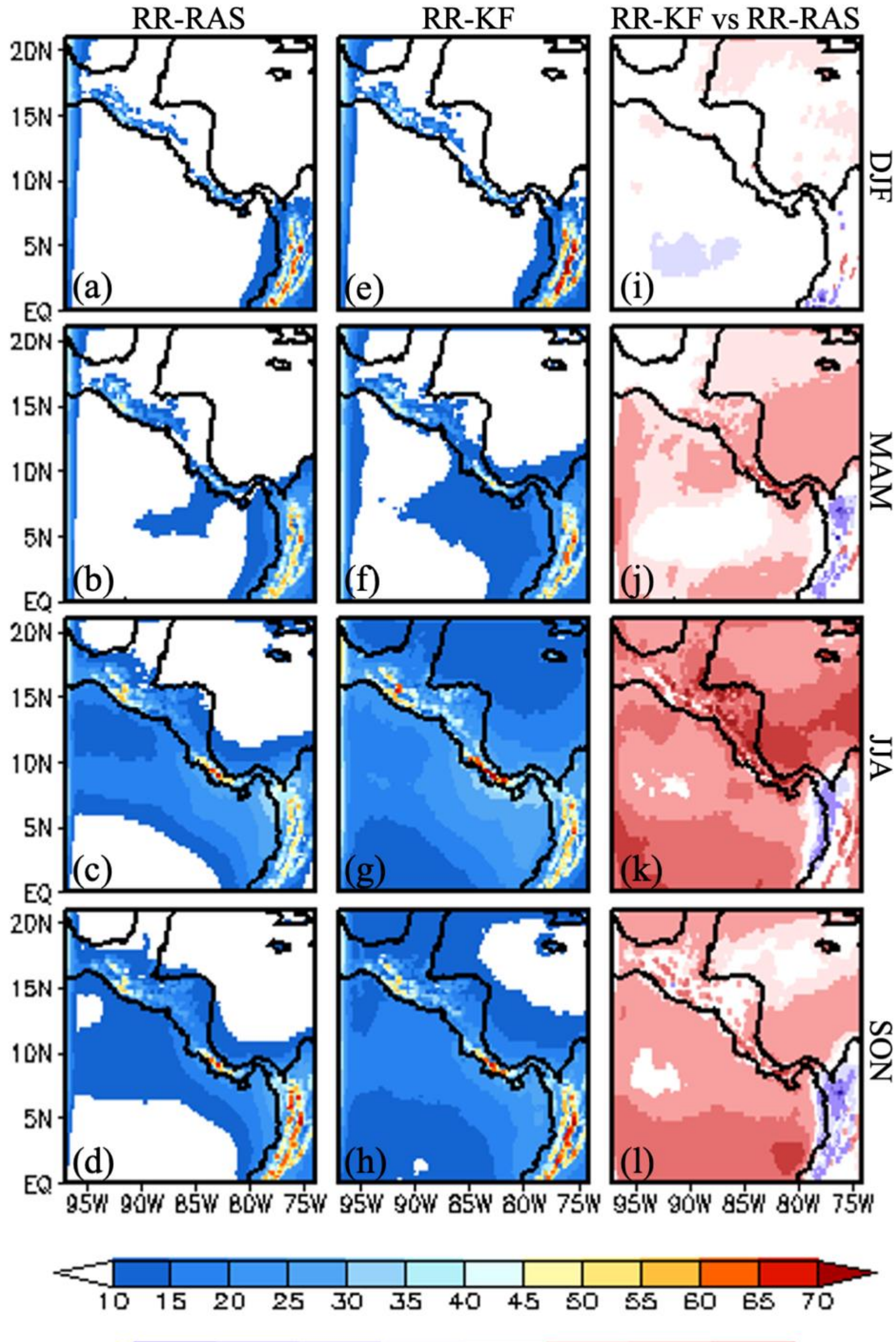

Figure S6: The seasonal mean climatological upper-level cloud cover (%; shaded) from (a, b, c, d) RR-RAS and (e, f, g, h) RR-KF2, and (i, j, k, l) corresponding difference of (RR-KF2) – (RR-RAS). The differences are shaded in (i, j, k, l) only if they exceed 95% confidence interval.

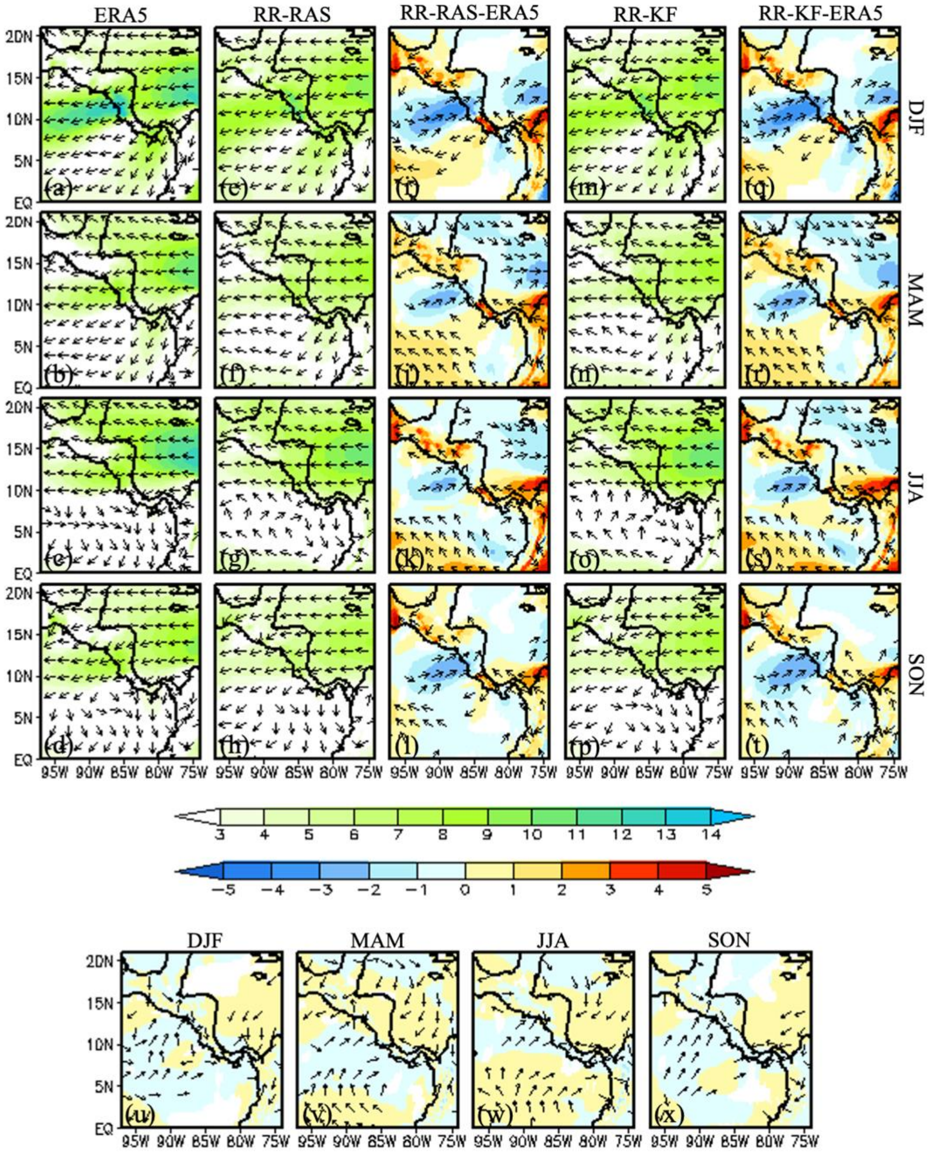

Figure S7: The seasonal mean 850 hPa winds (m s^{-1}) from (a, b, c, d) observations (ERA5) and (e, f, g, h) RR-RAS, (I, j, k, l) systematic errors of RR-RAS, (m, n, o, p) RR-KF2, (q, r, s, t) systematic errors of RR-KF2 and (u, v, w, x) difference of (RR-KF2) – (RR-RAS). The vectors are shown in (u, v, w, x) only if they exceed 95% confidence interval.

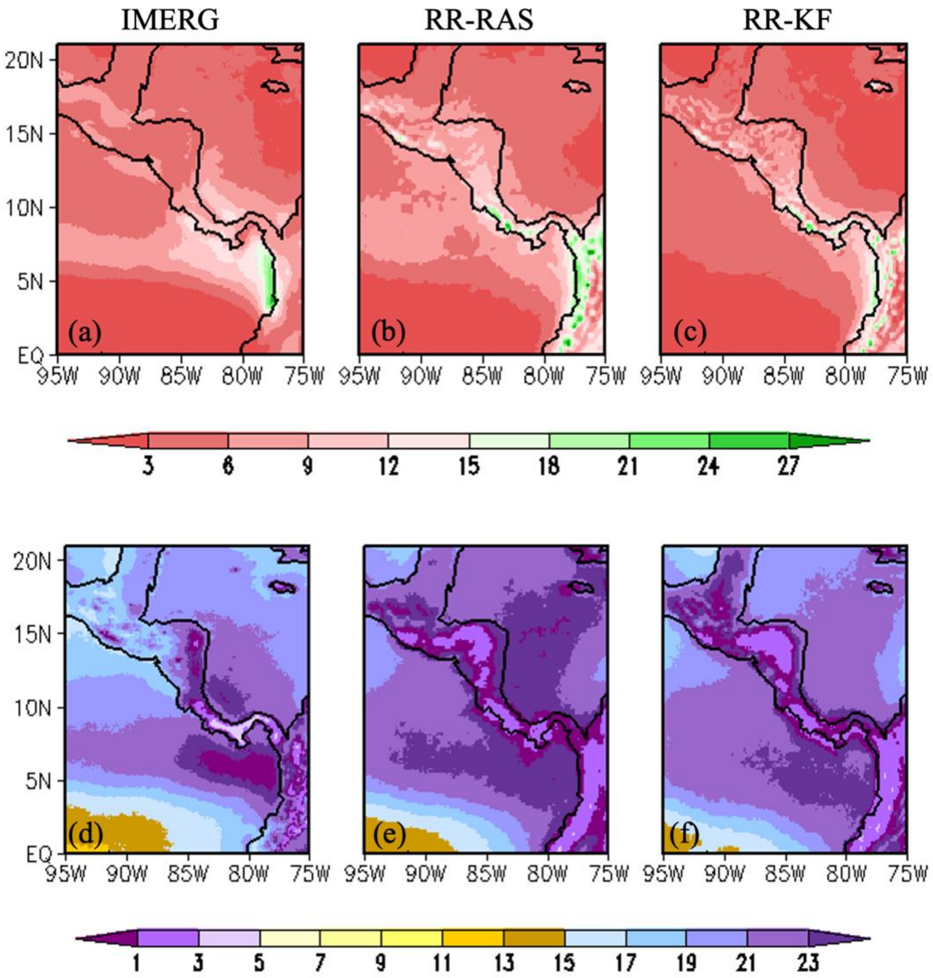

Figure S8: The mean SON climatological (a, b, c) diurnal amplitude (mm/day) and (d, e, f) phase of rainfall (LST) from (a, d) observations (IMERG), (b, e) RR-RAS, and (c, f) RR-KF2.